Far Infrared Spectroscopy of Heavy Fermion Superconductor CeCoIn$_5$

by

Stanislav Očadlík

Mgr. (Physics), Comenius University,
Bratislava, Slovakia, 1999

A THESIS SUBMITTED IN PARTIAL FULFILMENT OF
THE REQUIREMENTS FOR THE DEGREE OF

MASTER OF SCIENCE

in

The Faculty of Mathematics and Sciences

Department of Physics

BROCK UNIVERSITY

June 1, 2004

In presenting this thesis in partial fulfilment of the requirements for an advanced degree at the Brock University, I agree that the Library shall make it freely available for reference and study. I further agree that permission for extensive copying of this thesis for scholarly purposes may be granted by the head of my department or by his or her representatives. It is understood that copying or publication of this thesis for financial gain shall not be allowed without my written permission.

(Signature) _____

Department of Physics

Brock University
St.Catharines, Canada

Date _____

Abstract

The optical response to far infrared radiation has been measured on a mosaic of heavy fermion $CeCoIn_5$ single crystals. The superconducting transition temperature of the crystals has been determined by van der Pauw resistivity and ac-susceptibility measurements as $T_c = 2.3$ K. The optical measurements were taken above and below the transition temperature using a ^{3}He cryostat and step and integrate Martin-Puplett type polarizing interferometer.

The absolute reflectance of the heavy fermion $CeCoIn_5$ in the superconducting state in range $(0, 100)$cm^{-1} was calculated from the measured thermal reflectance, using the normal state data of Singley *et al* and a low frequency extrapolation for a metallic material in the Hagen-Rubens regime. By means of Kramers-Krönig analysis the absolute reflectance was used to calculate the optical conductivity of the sample.

The real part of the calculated complex conductivity $\sigma(\omega)$ of $CeCoIn_5$ indicates a possible opening of an energy gap close to 50 cm^{-1}.

Contents

List of Tables

List of Figures

Acknowledgements

I would like to thank my supervisor, Dr. Maureen Reedyk for her help, guidance, patience and time.

Special thanks to my fellow lab colleague, Sudhakar Gunuganti - for everything.

Another special "thank you" to Zuzana Tršková, for all the good times and for all of the photos in my thesis.

I would like to thank the members of the Physics Department for their support.

My special thanks to Dr. F. S. Razavi for the samples.

Another thank you to Panteha Razavi for the help with the susceptibility measurements.

Thanks to my Slovakian friends: Ivana Bosá, Vladimír Mundier and Henrich Ploczek, for making it easier to be here, and thanks to all my schoolmates and friends - Rob Klassen, Amir Keyvanloo, Mehdi Yazdanian, Graeme Wardlaw, Avid Farhoodfar, Helia Jalili, Talayeh Hezareh... for the atmosphere.

I thank my family for all their support.

I am very grateful for being the recipient of the Thompson-Harrison scholarship.

And I'd like to thank everyone who has made it easier to be here.

Chapter 1

Fourier Transform Infrared Spectroscopy

1.1 The Principle of Fourier Transform Spectroscopy

Fourier transform spectroscopy (FTS) is the technique of determining a spectrum by Fourier transformation (See Appendix A) of an interferogram (See Section 1.3.2), which is the record produced by a two-beam interferometer (See Section 1.3) as the path difference between the beams is varied from zero to some maximum value [1]. FTS is a well recognized method for analytic spectroscopic measurement in the UV, visible and infrared region. It is a measurement technique whereby spectra are collected based on the response from a pulse of electromagnetic radiation. It can be applied to a variety of types of spectroscopy including infra-red spectroscopy (FTIR), nuclear magnetic resonance, electron spin resonance spectroscopy, optical and mass spectrometry. Fourier transform spectroscopy is more sensitive and has a much shorter sampling time than conventional spectroscopic techniques [2, 3].

In a conventional (or "continuous wave") spectrometer, a sample is exposed to electromagnetic radiation and the response (usually the intensity of transmitted radiation) is monitored. The energy of the radiation is varied over the desired range and the response is plotted as a function of frequency (or radiation energy). At certain resonant

frequencies characteristic of the specific sample, the radiation will be absorbed resulting in a series of peaks in the spectrum, which can then be used to identify the sample [3].

Instead of varying the energy of the electromagnetic radiation, Fourier transform spectroscopy exposes the sample to a single pulse of radiation and measures the response. The resulting signal, called a free induction decay, contains a rapidly decaying composite of all possible frequencies. Due to resonance by the sample, resonant frequencies will be dominant in the signal and by performing a mathematical operation called a Fourier transform on the signal, the frequency response can be calculated. In this way the Fourier transform spectrometer can produce the same kind of spectrum as a conventional spectrometer, but in a much shorter time [3, 4].

The principles of the Fourier transform approach can be compared to the behavior of a musical tuning fork. If a tuning fork is exposed to sound waves of varying frequencies, it will vibrate when the sound wave frequencies are in "tune" (resonant frequencies). This is similar to conventional spectroscopic techniques, where the radiation frequency is varied and those frequencies, where the sample is in "tune" with the radiation, are detected. However, if we strike the tuning fork (the equivalent of applying a pulse of radiation), the tuning fork will tend to vibrate at its characteristic frequencies. The resulting tone consists of a combination of all of the characteristic frequencies for that tuning fork. Similarly, the response from a sample exposed to a pulse of radiation is a signal consisting primarily of the characteristic frequencies for that sample [3].

The mathematical technique for determining these characteristic frequencies from a single composite signal is Fourier transformation (FT). FT translates the signal from one domain to another one. In the case of optical spectroscopy, these domains are:

1) Time in seconds (the single composite signal as a time varying value)

2) Frequency in Hertz $[s^{-1}]$ (response measured as a function of all frequencies with non-zero amplitudes).

However, in interferometry (FTS) the typical domains used are space and inversed space (cm $\leftrightarrow$ cm^{-1}). This notation will also be used in this thesis. A simple example and basic mathematical overview of FT can be found in Appendix A.

1.2 Fourier Transform Infrared Spectroscopy

Infrared (IR) spectroscopy is one of the methodologies for investigating matter that has a very long history in research and applied sciences. This technique is capable of investigating many important phenomena in crystal lattices, such as phonons, magnons and charge carriers excitations, which involve very low energies. To excite and observe these kind of processes in solid matter, electro-magnetic radiation of appropriately low energy is needed. The energy range for many of these phenomena overlaps reasonably well with the energy range for IR radiation.

The infrared region of the electromagnetic spectrum lies approximately between the visible ($\lambda = 750$ nm) and microwave ($\lambda = 1$ mm) regions (see Figure 1.1). Infrared light

30 cm	1 mm	750 nm	400 nm	10 nm
Microwave	Infrared	Visible Light	UV Light	
4 μeV	1.3 meV	1.7 eV	3 eV	120 eV
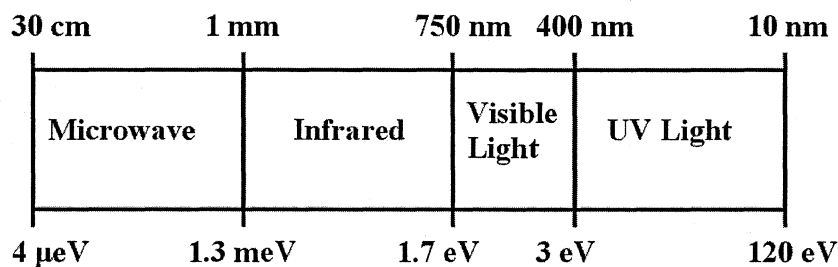
Figure 1.1: **IR light in electromagnetic spectrum**

is defined as a form of electromagnetic radiation with wavelengths between ~ 0.7 μm and 1 mm. These wavelengths are longer than those of visible light, but shorter than those of microwaves. (The prefix 'infra' means 'below'; infrared refers to radiation below the frequency of red light.) Infrared light is primarily thermal radiation, and we think of this as being heat. By convention, the infrared region is frequently divided into three

sections: Near-infrared (13300 - 4000cm^{-1}), Mid-IR (4000 - 400cm^{-1}) and Far-IR (400 - 10cm^{-1}). This division is not exact, but is widely used in the literature. In Table 1.1 we can see the IR range with respect to different units used in the field of IR spectroscopy.

Wavenumber [cm^{-1}]	Frequency [Hz]	Energy [eV]	Wavelength [m]
13300	4×10^{14}	1.65	750×10^{-9}
4000	1.2×10^{14}	0.5	2.5×10^{-6}
400	1.2×10^{13}	50×10^{-3}	25×10^{-6}
10	3×10^{11}	1.25×10^{-3}	1×10^{-3}

Table 1.1: **Range of IR light**

Radiation in this region can be utilized in structure determination by making use of the fact, that it is absorbed by interatomic bonds in the examined compounds and by their electron systems. (Especially Far-IR is highly useful for examination of optical and electronic properties of solids.) When a beam of infrared energy, covering a broad frequency range, passes through a sample, the energy at certain frequencies is absorbed by the sample. The IR absorption spectrum is characteristic of the particular molecule and its molecular motions and can be used for quantitative analysis of molecular systems and their electronic energy states. Chemical bonds in different environments will absorb varying intensities at varying frequencies.

At very low temperatures (*e.g.* 4 K), IR spectra are very sensitive to the presence of small amounts of impurities in the material of the sample being studied. Because the region of interest is of such low energy, special apparatus (He cryostat) is required to allow for maximum detection and to cool the ambient temperature below transition temperatures. To carry out the measurements by means of low temperature apparatus is also necessary because of the presence of a strong IR background signal at high temperatures

(*i.e.* IR noise). The details regarding the apparatus for low temperature measurements can be found in Chapter 3.

Although British astronomer William Herschel discovered the existence of IR radiation in the electromagnetic spectrum for the first time around 1800 [5], and Albert Michelson built his first interferometer in 1881 [6], the application of this technology required almost a century before it revolutionized IR spectroscopy as we know it. The introduction of computers in the second half of the 20th century allowed the digitization of the interference information (called an interferogram) followed by fast Fourier transformation (FFT) of the data into the actual IR spectrum.

The usually mentioned benefits of interferometry over dispersive measurements are: FTIR spectroscopy is much faster and more sensitive (the multiplex or Felgett advantage - see Section 1.3.3); it uses all IR energies simultaneously, thereby achieving much lower noise levels (the throughput or Jacquinot advantage - see Section 1.3.4), and an internal laser calibrates the interference information, providing very high wavenumber accuracy and reproducibility (the precision or Connes advantage - see Section 1.3.5). In addition, no stray light is generated by interferometry, which leads to more accurate quantitative results than is possible with dispersive technologies. Interferometric techniques greatly enhance the speed and sensitivity at which this type of spectroscopy is conducted. The measurement devices working on the principle of FTS are Fourier transform spectrometers.

1.3 A Fourier Transform Spectrometer

A Fourier transform spectrometer is a Michelson interferometer (sometimes refered to as two-beam interferometer) with a movable mirror. By scanning the movable mirror over some distance, an interference pattern is produced that encodes the spectrum of the source (in fact, it is its Fourier transform) [6].
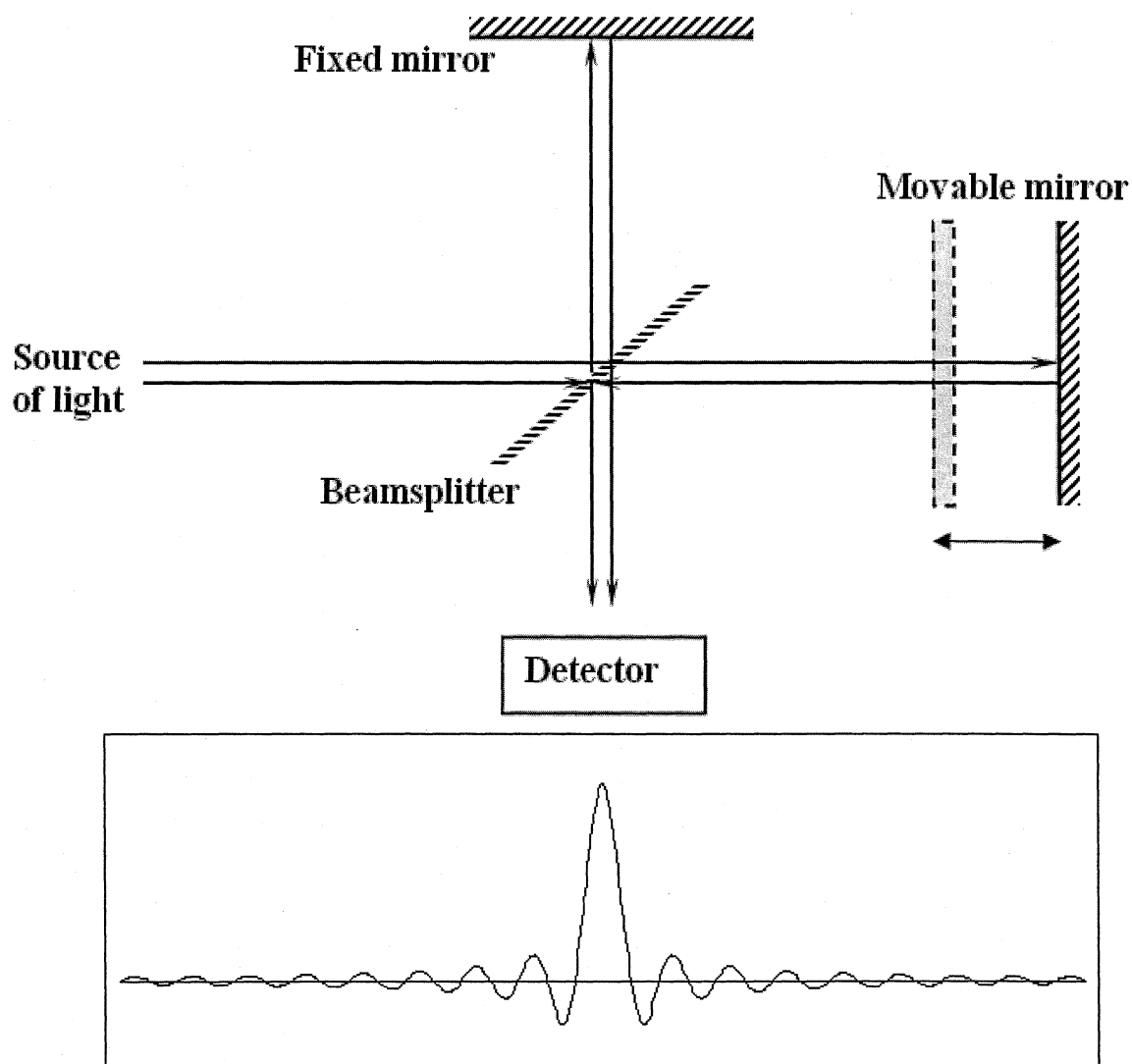
Figure 1.2: The scheme of a Michelson interferometer and its theoretical interferogram of a composite pulse

Figure 1.2 shows a simplest form of a Fourier transform spectrometer. It consists of two mirrors, one fixed and one movable, located at a right angle to each other (oriented perpendicularly), with a beam splitter placed at the vertex of the right angle and oriented at a 45° angle relative to the two mirrors. The beam splitter is made of a special material that transmits half of the radiation striking it and reflects the other half. (This would be true in a case of an ideal beam splitter without any frequency dependence for reflectance and transmittance, the reality is of course different.) Radiation from the source strikes the beam splitter and separates into two beams. One beam is transmitted through the beam splitter to the moving mirror and the second is reflected off the beam splitter to the fixed mirror. The fixed and moving mirrors reflect the radiation back to the beamsplitter. Again, half of this reflected radiation is transmitted and half is reflected at the beam splitter, resulting in one beam passing to the detector and the second back to the source. When the position of movable mirror is continuously varied along the axis of the corresponding arm, an interference pattern is swept out as the two phase-shifted beams interfere with each other [6].

1.3.1 OPD and ZPD

Optical Path Difference (OPD) is the optical path difference between the beams travelling through the two arms of an interferometer. OPD is equal to the product of the physical distance travelled by the moving mirror (multiplied by 2, 4, or other multiplier which is a function of the number of reflecting elements used; for the simplest case seen on Figure 1.2 this multiplier is 2) and n, the index of refraction of the medium filling the interferometer arms (air, Nitrogen for purged systems, etc...) [7]. The raw FT-IR data consists of a number of (signal, OPD) pairs of values. FT-IR spectrometer has a natural reference point when the moving and fixed mirrors are the same distance from the beam splitter. This condition is called zero path difference or ZPD. The moving mirror displacement,

d, is measured from the ZPD. The relationship between the optical path difference and the mirror displacement for the simplest form is

$$OPD = 2dn \tag{1.1}$$

1.3.2   The Interferogram

Interferogram is the name given to the signal format acquired by an FT-IR spectrometer. It is usually significantly more complex looking than a single sinusoid, which would be expected if only a single wavelength of light was present. The centerburst, the big spike in the centre of Figure 1.2 is a telltale signature of a broadband source. Its origin lies in the fact that all wavelengths are in phase at the ZPD. Therefore, their contributions are all at maximum and a very strong signal is produced by the system's detector. As the OPD grows, different wavelengths produce peak readings at different positions and, for a broadband signal, they never reach their peaks at the same time. Thus, as you move away from centerburst, the interferogram becomes a complex looking oscillatory signal with decreasing amplitude [7].

1.3.3   The Multiplex (Fellgett) Advantage

In a dispersive spectrometer, wavenumbers are observed sequentially, as the grating is scanned. In an FT-IR spectrometer, all wavenumbers of light are observed at once. When spectra are collected under identical conditions (spectra collected in the same measurement time, at the same resolution, and with the same source, detector, optical throughput and optical efficiency) on dispersive and FT-IR spectrometers, the signal-to-noise ratio of the FT-IR spectrum will be greater than that of the dispersive IR spectrum by a factor of $\sqrt{M}$, where M is the number of resolution elements [8]. This factor arises due to the fact, that a single detector is used to detect all of the frequencies in the source simultaneously. The noise produced in this one detector is therefore shared equally by

all of the recorded signals. If M frequencies are measured in the spectrum, we would ordinarily use M detectors to measure the spectrum and in the process get M samples of the noise. The spectrum recorded by the interferometer, however, has only one detector and as a result has $\sqrt{M}$ less noise, than its dispersively measured counterpart [4].

1.3.4 The Throughput Advantage

FT-IR instruments do not require slits (in the traditional sense) to achieve resolution. Therefore, you get much higher throughput with an FT-IR than you do with a dispersive instrument. This is called the Jacquinot Advantage. In reality there are some slit-like limits in the system, due to the fact that one needs to achieve a minimum level of collimation of the beams in the two arms of the interferometer for any particular level of resolution [7, 8].

1.3.5 HeNe laser in FT Spectrometer - Precision Advantage

A collimated monochromatic light source will produce an interferogram in the form of a sinusoid at the detector. When the light intensity goes from one maximum of the interferogram to the next maximum, the optical path difference between the two legs of the interferometer changes by exactly the wavelength of the incoming radiation.

The straightforward utilization of this fact has led to the development of FT spectrometers with presence of HeNe lasers. A HeNe laser emits light with a wavelength of 633 nm, which is known with a very high degree of accuracy and which does not significantly change under any common circumstances. The laser beam parallels the signal path through the interferometer and produces its own interferogram at a separate detector. This signal is used as an extremely accurate measure of the interferometer displacement (OPD). It is observed as a sinusoidal signal. The average value is half the value you would see if the beams were not divided and no interference produced. The

sinusoid goes positive and negative about this value. The average signal level is called zero level. A high precision electronic circuit produces a voltage pulse when the HeNe reference sinusoid crosses zero level. By use of only positive zero crossing, the circuitry can develop one pulse per cycle of the interferogram, or use all zero crossings for two pulses per cycle of the interferogram. The latter case is often called oversampling [7].

There is a fundamental rule called the Nyquist Theorem which can be paraphrased to state that a sinusoid can be restored exactly from its discrete representation if it has been sampled at a frequency at least twice as high as its own frequency. If we apply this rule we find that the minimum value of lambda is twice the wavelength of the reference laser:

$$\lambda = 633nm * 2 = 1.266\mu m \tag{1.2}$$

With oversampling, the reference laser wavelength is effectively halved. So in this case:

$$\lambda = (633nm/2) * 2 = 633nm \tag{1.3}$$

In practice, the FFT math runs into difficulties close to the theoretical limit. That is why we say 1.4μm is the limiting wavelength without oversampling, and 700nm is the limiting wavelength with oversampling [7].

1.3.6 How a FT-IR spectrometer works

In a two-beam interferometer the position of the movable mirror varies linearly with time. This motion at constant speed allows the OPD to increase linearly, and the two beams create an interference pattern (interferogram). The interferogram measures the intensity as a function of the movable mirror position. The intensity detected of these two plane waves can be expressed as

$$I = |\vec{E}|^2 = |\vec{E_1}|^2 + |\vec{E_2}|^2 + 2\vec{E_1} \cdot \vec{E_2}\cos\theta \tag{1.4}$$

In the case of normal incidence of both beams in the optical system, the relation between the angle θ, the wavenumber k_0 and the optical path difference x is very simple

$$\theta = k_0 x \tag{1.5}$$

Providing that the beam-splitter is ideal and the electric field intensities of both waves are equal and we can set them to $G_0/2$ for the brevity, then

$$I(x) = G_0(1 + \cos k_0 x) \tag{1.6}$$

The intensity is a function of the path difference, as expected, and in this case there is only one inherent wavenumber k_0 (monochromatic source). Similarly, for a polychromatic continuous source, the resultant intensity can be written as

$$I(x) = \int_0^\infty [1 + \cos kx] G(k) dk \tag{1.7}$$

which can be rearranged to

$$I(x) = \int_0^\infty G(k) dk + \int_0^\infty G(k) \frac{e^{ikx} + e^{-ikx}}{2} dk = \frac{1}{2} I(0) + \frac{1}{2} \int_{-\infty}^\infty G(k) e^{ikx} dk \tag{1.8}$$

Theoretically, there is no such thing as negative values for k. However, it is convenient to write the interferogram function over symmetric, infinite limits. We can rewrite the latter formula to a more familiar form, used in spectroscopy

$$W(x) = \frac{2I(x) - I(0)}{\sqrt{2\pi}} = \frac{1}{\sqrt{2\pi}} \int_{-\infty}^\infty G(k) e^{ikx} dk \tag{1.9}$$

Which can be quickly recognized as a Fourier transform! The detected intensity as a function of moving mirror position $I(x)$ can therefore be converted into $G(k)$, the intensity spectrum as a function of frequency by a simple Fourier transform.

$$G(k) = \frac{1}{\sqrt{2\pi}} \int_{-\infty}^\infty W(x) e^{-ikx} dx \tag{1.10}$$

The FT works here as a tool capable of changing the experimental information expressed in one domain to another. The Fourier analysis is used to transform the interferogram to a plot of intensity as a function of frequency (or wavenumber). Such a plot is called a power spectrum.

1.3.7 Finite Resolution

In practice one cannot measure the OPD from $-\infty$ to $+\infty$. The resolution of a measurement is simply given by how far in x you measure. It is fairly simple to illustrate conceptually how the resolution of a spectrum measured interferometrically depends on the maximum retardation of the scan. The following discussion of the resolution is done according to Griffiths [8]. As an example, let us consider the case of a spectrum consisting of a doublet, both components of which have equal intensity. Figure 1.3 shows these two waves and their interferogram.
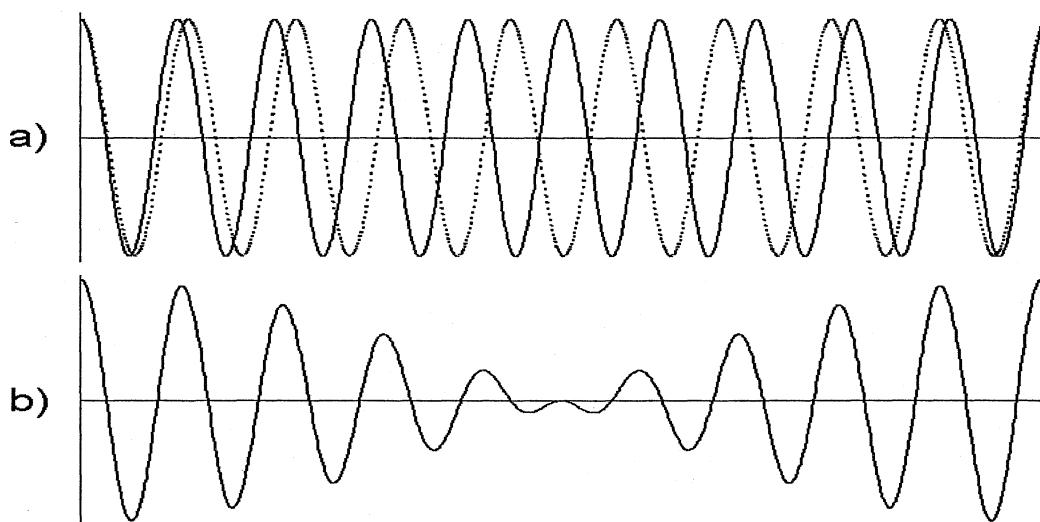
Figure 1.3: a) **Two close waves; solid line - $10\lambda_1$, dashed line - $9\lambda_2$**

b) **Interferogram with the its first maximum**

If the doublet has a separation of $\Delta k(=k_1 - k_2)$, the two cosine waves become completely out of phase after a retardation of $0.5(\Delta k)^{-1}$, and are once more back in phase after a retardation of $(\Delta k)^{-1}$. To go through one complete period of the beat frequency, a retardation of $(\Delta k)^{-1}$ is therefore required. (An interferogram measured only to half of this retardation could not be readily distinguished from the interferogram of a source

with a Lorentzian profile [8].) The narrower the separation of the doublet, the greater is the retardation before the cosine waves become in phase. It is therefore apparent, that the spectral resolution depends on the maximum retardation of the interferometer. Intuitively it might be concluded that the two lines could just be resolved, if the retardation were increased to the point where the two waves became in phase for the first time after zero retardation. As we can see in Figure 1.3, the two waves become in phase for the first time after zero retardation point when

$$\delta = (\Delta k)^{-1} \tag{1.11}$$

Thus, if the maximum retardation of an interferometer is Δ_{max}, the best resolution that could be obtained using this interferometer Δk, is given by

$$\Delta k = (\Delta_{max})^{-1} \tag{1.12}$$

Although this conclusion was arrived at intuively, the answer proves to be approximately correct [8].

1.3.8   Sampling Frequency and Cut-off Frequency

In order to compute the complete spectrum from (0 to $+\infty$) cm^{-1} the interferogram would have to be sampled at infinitesimally small increments of retardation. This is, of course, impossible, at very least because it would create an infinite experimental data set. As has been already mentioned in section 1.3.5 a sinusoidal function of time (or distance) can be unambiguously sampled using a sampling frequency greater than or equal to twice the maximum frequency in the function. If we consider the case with oversampling (see section 1.3.5), then the increment of retardation for the movable mirror is ~ 317 nm and the wavelength limit for the measured signal is 633 nm (see equation 1.3). Using a simple relation for the wavenumber

$$\nu = \frac{1}{\lambda} \tag{1.13}$$

will give us the maximum or so-called cut-off frequency $\nu_{max} = 15797$ cm^{-1}.

1.3.9 Apodization

The range of data elements collected by a spectrometer is always finite (subject to Δ_{max} or the resolution chosen) but, as we have seen, the Fourier transformation itself assumes this range to be infinite. In practice the spectrometer "truncates" the range of data by recording the measured signal up to some finite OPD. From a mathematical point of view this is equivalent to multiplying the infinite series of data with a "boxcar" function, that is, a function that is one over the time period for which data are collected, and zero before and after this period. To the transformed spectra, this is the convolution of the boxcar function with the original data [4]. The relation for the Fourier transformation then changes

$$G(k) = \frac{1}{\sqrt{2\pi}} \int_{-\infty}^{\infty} W(x)B(x)e^{-ikx}dx \qquad (1.14)$$

where

$$B(x) = \begin{cases} 1 & \text{for } -\Delta \leq x \leq \Delta \\ 0 & \text{Otherwise} \end{cases} \qquad (1.15)$$

is the boxcar function. The most important consequence of this convolution is the so called Gibbs phenomenon, a phenomenon occurring whenever a curve with sharp edges (B(x) in this case) is subject to Fourier transformation, resulting in a change in frequency representation in the transformed signal. This arises from the fact, that the representation of the profilers measured with a limited number of Fourier harmonics is imperfect and is resulting in high frequency oscillations at the edges. To cure this imprecision, special data processing known as apodization (literally "foot removing") is performed on the data prior to transformation [4]. The data are usually multiplied by some smooth function to ensure that they go to zero at the edges of the data set. An example of such a function

is the triangular apodization function

$$A_1(x) = \begin{cases} 1 - \frac{|x|}{\Delta} & \text{for } -\Delta \leq x \leq \Delta \\ 0 & \text{Otherwise} \end{cases} \qquad (1.16)$$

This is a commonly used function in IR Fourier transform spectrometry. It suppresses the magnitude of the side lobes of an interferogram and helps to decrease the influence of the finite Δ on the real shape of the measured signal. (For more apodization functions see for example Griffiths [8].)

Chapter 2

The Optical Reflectance and Kramers-Kronig Analysis

The knowledge of optical material properties is essential for many materials and measurements of light reflected by the sample can provide us with a great deal of information about the electron systems in the solid [9]. Reflectance spectroscopy provides a powerful and versatile tool for optical characterization of solid matter. The spectroscopic measurement is used to obtain optical functions from a spectroscopic measurement in conjunction with the so called Kramers-Kronig analysis. Kramers-Kronig relations (KKR) can be derived by applying the Cauchy integral formula (Appendix B) to an analytic function bounded in the entire upper half-plane of its complex argument. They express the interdependence between the real and the imaginary parts of such a function [10, 11].

2.1 The Optical Reflectance

Measurements of the reflectivity of light at normal incidence on a single crystal can provide much information concerning the electronic system. The experimentally obtained reflectance is defined as the unitless fraction

$$R(\omega) = r^*(\omega)r(\omega) = \rho^2(\omega) = \frac{E_{ref}^* E_{ref}}{E_{inc}^* E_{inc}} \tag{2.1}$$

where $\rho(\omega)$ is the complex reflectivity amplitude and E_{inc} and E_{ref} are the incident and reflected electric fields, respectively [9]. The reflectivity coefficient r(ω) is a complex

function defined at the crystal surface as the ratio of the reflected electric field to the incident electric field

$$r(\omega) \equiv \frac{E_{ref}}{E_{inc}} \equiv \rho(\omega)e^{i\theta(\omega)} \tag{2.2}$$

where we have separated amplitude $\rho(\omega)$ and phase $\theta(\omega)$ parts [9].

From the interaction of electromagnetic radiation with matter at normal incidence it can be shown (see Appendix C), that quantities such as:

- complex index of refraction N(ω), [N(ω) = n + ik]

- complex dielectric constant ϵ, [$\epsilon = \epsilon_1 + i\epsilon_2$]

- complex conductivity σ, [$\sigma = \sigma_1 + i\sigma_2$]

are related to the optical reflectance R(ω) and reflectivity coefficient r(ω) via the following relations

$$r(\omega) = \frac{N-1}{N+1} = \frac{n+ik-1}{n+ik+1} \tag{2.3}$$

$$R(\omega) = \frac{(n-1)^2 + k^2}{(n+1)^2 + k^2} \tag{2.4}$$

$$N(\omega) = \sqrt{\epsilon(\omega)} \tag{2.5}$$

$$\epsilon(\omega) = 1 + i\frac{\sigma}{\epsilon_0 \omega} \tag{2.6}$$

where we assume that the light propagates from empty space into a medium with index of refraction N, and in equation 2.5 and equation 2.6 that the relative magnetic permeability $\mu_{rel} = 1$. It is generally difficult to determine N, $\epsilon(\omega)$ and $\sigma(\omega)$ directly. In measuring the reflectance of the crystal R(ω) (or more specifically measuring the reflected power of the EM wave), we are measuring a real quantity, that holds implicitly the index of refraction, dielectric function and conductivity [12].

As one can recognize from equation 2.1, from R(ω) it is possible to find out the amplitude part $\rho(\omega)$ of r(ω), yet it is impossible to determine its phase part $\theta(\omega)$, which

is crucial for extracting both the real and imaginary components of the complex index of refraction. Fortunately, there is a mathematical method that helps us deal with this problem, as is shown in the following section.

2.2   Linear Response and Kramers-Kronig Relations

When a solid material is exposed to an electric field E, there is a polarization P generated in response to the applied field. This linear response of a medium to an electric stimulus (*e.g.* infrared beam) can be expressed as

$$P(t) = \epsilon_0 \int_{-\infty}^{\infty} \chi_e(t - t')E(t')dt' \tag{2.7}$$

where $\chi_e(t-t')$ is the response function of the medium after an electric field $E(t')$ has been applied at time t' and ϵ_0 is the permitivity of vacuum [10]. After Fourier transforming each of the functions involved, equation 2.7 can be rewritten in the frequency domain as

$$P(\omega) = \epsilon_0 \chi_e(\omega)E(\omega) \tag{2.8}$$

which explicitly expresses the linear response of a medium to a harmonic component of an electro-magnetic wave. The electric susceptibility $\chi_e(\omega)$ is analytic and bounded in the upper half-plane of the complex angular frequency argument. This can be deduced after applying the causality principle [13], i. e. $\chi_e(t - t') = 0$ for $t < t'$, with the expression for closed-contour integral around the upper half-plane when evaluating the Fourier transform of this function

$$\chi_e(t - t') = \frac{1}{2\pi} \int_{-\infty}^{\infty} \chi_e(\omega)e^{-i\omega(t-t')}d\omega \tag{2.9}$$

Application of the Cauchy integral formula on $\chi(\omega)$ yields the following equation

$$\chi_e(\omega) = \frac{i}{\pi} P \int_{-\infty}^{\infty} \frac{\chi_e(\omega')}{\omega' - \omega}d\omega' \tag{2.10}$$

and after separating its complex components (subscripts r and i will be used for the real and imaginary parts, respectively) we obtain

$$\chi_r(\omega) = \frac{1}{\pi} P \int_{-\infty}^{\infty} \frac{\chi_i(\omega')}{\omega' - \omega} d\omega' \tag{2.11}$$

$$\chi_i(\omega) = -\frac{1}{\pi} P \int_{-\infty}^{\infty} \frac{\chi_r(\omega')}{\omega' - \omega} d\omega' \tag{2.12}$$

ω and ω' are real and independent values of the angular frequency and P denotes the Cauchy principal value of the integral. This pair of equations is called Kramers-Kronig, due to their originators. They relate the real (dissipative) part with the imaginary (absorptive) part of the susceptibility and are also referred to as dispersion relations [10].

Function $\chi_e(t - t')$ is a real quantity. From eqn. 2.10 then follows

$$\chi_e(-\omega) = \chi_e^*(\omega) \tag{2.13}$$

where χ_e^* denotes the complex conjugate. Consequently equations 2.11 and 2.12 reformulated for positive values of frequency read

$$\chi_r(\omega) = \frac{2}{\pi} P \int_0^{\infty} \frac{\omega' \chi_i(\omega') - \omega \chi_i(\omega)}{\omega'^2 - \omega^2} d\omega' \tag{2.14}$$

$$\chi_i(\omega) = -\frac{2}{\pi} P \int_0^{\infty} \frac{\chi_r(\omega') - \chi_r(\omega)}{\omega'^2 - \omega^2} d\omega' \tag{2.15}$$

Equivalently they can be written for other material parameters, like the complex dielectric function $\epsilon(\omega) = \epsilon_1(\omega) + i\epsilon_2(\omega)$ after substituting $\chi_e(\omega) = \epsilon(\omega) - 1$, or the complex index of refraction $N(\omega) = n(\omega) + ik(\omega)$, for which $N^2(\omega) = \epsilon(\omega)$.

Neither of the above mentioned parameters is directly experimentally accessible. For this purpose a reflectance measurement is commonly used. The expression for the reflection coefficient at normal incidence $r(\omega)$ is

$$r(\omega) = \frac{E_{ref}(\omega)}{E_{inc}(\omega)} = \frac{n(\omega) - 1 + ik(\omega)}{n(\omega) + 1 + ik(\omega)} \tag{2.16}$$

E_{ref} and E_{inc} are electric field strength magnitudes in the reflected and incident beams, respectively. The measured quantity of reflectance $R(\omega)$ equals the square of its modulus,

hence in polar form

$$r(\omega) = \sqrt{R(\omega)}e^{i\theta(\omega)} \qquad (2.17)$$

and

$$\ln r(\omega) = \frac{1}{2}\ln R(\omega) + i\theta(\omega) \qquad (2.18)$$

The corresponding pair of Kramers-Kronig relations reads [10]

$$\ln R(\omega) = \frac{2}{\pi}P\int_{-\infty}^{\infty}\frac{\theta(\omega')}{\omega' - \omega}d\omega' \qquad (2.19)$$

$$\theta(\omega) = -\frac{1}{2\pi}P\int_{-\infty}^{\infty}\frac{\ln R(\omega')}{\omega' - \omega}d\omega' \qquad (2.20)$$

These hold under the condition that $ln(r(\omega))$ is analytic and bounded in the upper half-plane of the complex frequency argument. Applying the same arguments as with the susceptibility above, the last equation in the positive frequency domain reads

$$\theta(\omega) = -\frac{\omega}{\pi}P\int_{0}^{\infty}\frac{\ln R(\omega')}{\omega'^2 - \omega^2}d\omega' \qquad (2.21)$$

This is the form that can be used to retrieve the phase spectrum from the measured reflectance spectrum and hence all the related material optical functions. For example, from equations 2.16 and 2.17 we can relate R and θ with real refractive index n and the extinction coefficient k [14] (see App. C)

$$n = \frac{1 - R}{1 - 2\sqrt{R}\cos\theta + R} \qquad (2.22)$$

$$k = \frac{2\sqrt{R}\sin\theta}{1 - 2\sqrt{R}\cos\theta + R} \qquad (2.23)$$

2.2.1 Extrapolations for Reflectance

Equation 2.21 extends over the frequency range from 0 to $+\infty$ and thus extrapolation must be used in the ranges, where the experimental data cannot be obtained [10]. The

most common approach is to assume, that above the valence electron plasma frequency ω_p the dielectric function is given by the Drude formula [15]

$$\epsilon(\omega) = 1 - \frac{\omega_p^2}{\omega^2} \qquad (2.24)$$

where

$$\omega_p^2 = \frac{Ne^2}{m\epsilon_0} \qquad (2.25)$$

is the plasma frequency and N is the number of electrons per cm^3.

Thus at high frequencies $\epsilon_r \approx 1$, $\epsilon_i \approx 0$ and $k \approx 0$ (extinction coefficient) so that

$$n = \sqrt{\epsilon} \approx 1 - \frac{1}{2}\frac{\omega_p^2}{\omega^2} \qquad (2.26)$$

and

$$R(\omega) = \frac{(1-n)^2}{(1+n)^2} \approx \frac{1}{16}\frac{\omega_p^4}{\omega^4} \qquad (2.27)$$

If the upper measurement frequency limit ω_1 is larger than ω_p, $R(\omega)$ can be extrapolated beyond ω_1 by

$$R(\omega) = R(\omega_1)(\frac{\omega_1}{\omega})^4, \qquad (2.28)$$

and its contribution to the KK integral can be evaluated analytically.

Another extrapolation must be done in the low frequency range (down to the zero frequency). In a metallic material one usually invokes the so-called Hagen-Rubens (HR) reflectance. It arises in the low frequency (or HR) regime defined by the condition $\omega\tau << 1$, where $\tau = 1/\gamma$, and γ can be interpreted as a scattering rate in the damped harmonic oscillator model for the conduction electrons. (For more details see for example Dressel [49].) In this regime the optical properties are mainly determined by the dc conductivity of the material. In the low frequency limit the real and imaginary parts of the complex refractive index can be considered equal with a high precision. Thus we have

$$n = k \qquad (2.29)$$

and we can rewrite equation 2.4 by neglecting all the terms of higher order than 2

$$R \approx 1 - \frac{2}{n} \tag{2.30}$$

which can be reformulated to

$$R \approx 1 - 2(\frac{2\epsilon_0\omega}{\sigma_{dc}})^{1/2}. \tag{2.31}$$

This is called the Hagen-Rubens reflectance.

2.3 Experimental Optical Reflectance

The optical reflectance is defined as the ratio of the intensity of the beam incident on a sample to that of the beam reflected from the sample. To know both of these physical quantities the following procedure is used.

The IR light coming from a source is incident on the measured sample, and then on a reference mirror. The reference mirror acts as an intrarun reference, correcting any signal drifts, that can occur during the experiment. The RATIO is obtained [16] by dividing the power spectra of measured signals (sample and reference), i.e. after the Fourier transform of corresponding interferograms. Another step is to correct possible scattering effects and any unwanted interference due to the surface imperfections. The sample is used as its own reference via an in-situ gold evaporation. The amount of gold used is small enough to maintain the same surface topology of the sample. Gold is used here because of its high reflectivity in the FIR and the negligible temperature dependence of its $R(\omega)$. The same measurements are carried out on the coated sample, as on the uncoated sample. New ratio between the mirror and the coated sample is then obtained. Let's call this ratio GOLD-RATIO [16]. The final step is to divide RATIO with GOLD-RATIO and multiply it with the reflectance of gold, which is a known function, where the result can be represented as [16]

$$|Reflectance| = \frac{RATIO}{GOLD - RATIO} \times (\text{known reflectance of gold}) \tag{2.32}$$

or

$$|R| = \frac{\left(\frac{sample\ reflectance}{mirror\ reflectance}\right)}{\left(\frac{gold\ reflectance}{mirror\ reflectance}\right)} \times (\text{known reflectance of gold}) \qquad (2.33)$$

This yields the absolute reflectance of the measured sample.

Chapter 3

The Experimental Apparatus for FIR Spectroscopy

3.1 The Martin-Puplett Interferometer

The interferometer used for experiments is one of the Martin-Puplett variety. The basic difference between the Martin-Puplett interferometer (MPI) and the Michelson type of interferometers is, that the MPI is working with polarized light. The scheme of the MPI is shown in Figure 3.1.

The infrared beam source in this interferometer is a Hg-Xe arc lamp. After several reflections (M1 → M3) it hits the polarizer (P1), which polarizes the light horizontally. The horizontally polarized light hits the 45° polarizing beam splitter, which transmits half of the light and reflects other half. The transmitted and reflected beams hit the two roof mirrors (RM1, RM2) where they are reflected and their polarizations switched, the initially transmitted beam is reflected, while the initially reflected beam is transmitted at the beam splitter, and the two beams recombine. The resulting (recombined) beam travels to two other mirrors (M4, M5) and then reaches a polarization modulator (C2) before it exits the interferometer. This modulator (C2) acts like a chopper and allows a lock-in amplifier to be used to detect the signal, so that background noise may be reduced.

Legend:

BS Beam Splitter
C_1 Chopper
C_2 Polarizing Chopper
I Iris
L Hg–Xe Lamp
M_1 Concave Mirror
M_2 & M_4
  Flat Mirror
M_3 & M_5
  Paraboloidal Mirror
RM_1 & RM_2
  Roof Mirror
P_1 Polarizer
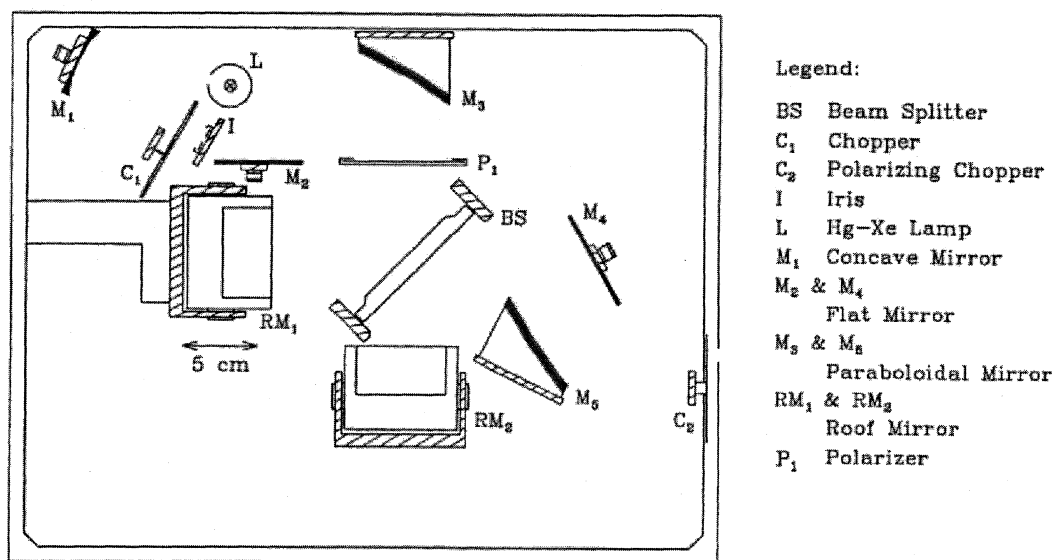
Figure 3.1: **The scheme of a Martin-Puplett interferometer** [16]

3.2 The ^{3}He Cryostat

The cryostat used for the experiments is the model HDL-10 dewar with dual ^{3}He refrigerators from Infrared Laboratories. This system features two independent ^{3}He refrigerators. It is possible to use both of them, or just one. During the experiment one of this refrigerators is used for the IR sensor, and the other one for the examined sample.

There are two main reasons why one uses a cryostat. First of all, when running a spectroscopy measurement in the FIR region, it is necessary to suppress the strong IR noise, which is present at common ambient temperatures. The FIR detector used for the experiments, called a bolometer, is a very sensitive device, capable of measuring slight differences in FIR light incident on it. It measures the temperature change, when a photon hits its surface. Therefore, it must be maintained at a constant temperature. The temperature used in the experiments was approximately 0.37 K. This very low working

temperature assures, that the recorded signal is due to the IR light reflected from the sample, and it also suppresses thermal noise inside the detector itself. (More details about the bolometer can be found in section 3.3)

The second reason a cryostat is used, is to be able to run experiments on the sample at low temperatures. This goal is achieved by controlling (changing) the temperature at the sample stage of the cryostat, while keeping the bolometer stage cooled down. A schematic overview of the ^{3}He cryostat is shown in Figure 3.2.

Legend:

AF	Absorption Foam
BM	Bolometer
CC	Charcoal Pump
CP	Helium-4 Cold Plate
DC	Dewar Case
HC	Helium-3 Cold Plate
HT	Helium-3 Tank
LP	Light Pipes
PA	Preamplifier
PF	Polyethylene Filters
BF	Bolometer Filter
PL	Polyethylene Lenses
PW	Polyethylene Windows
RS	Radiation Shield
SA	Sample
SH_1	Shutter for Sample
SH_2	Shutter for Reference
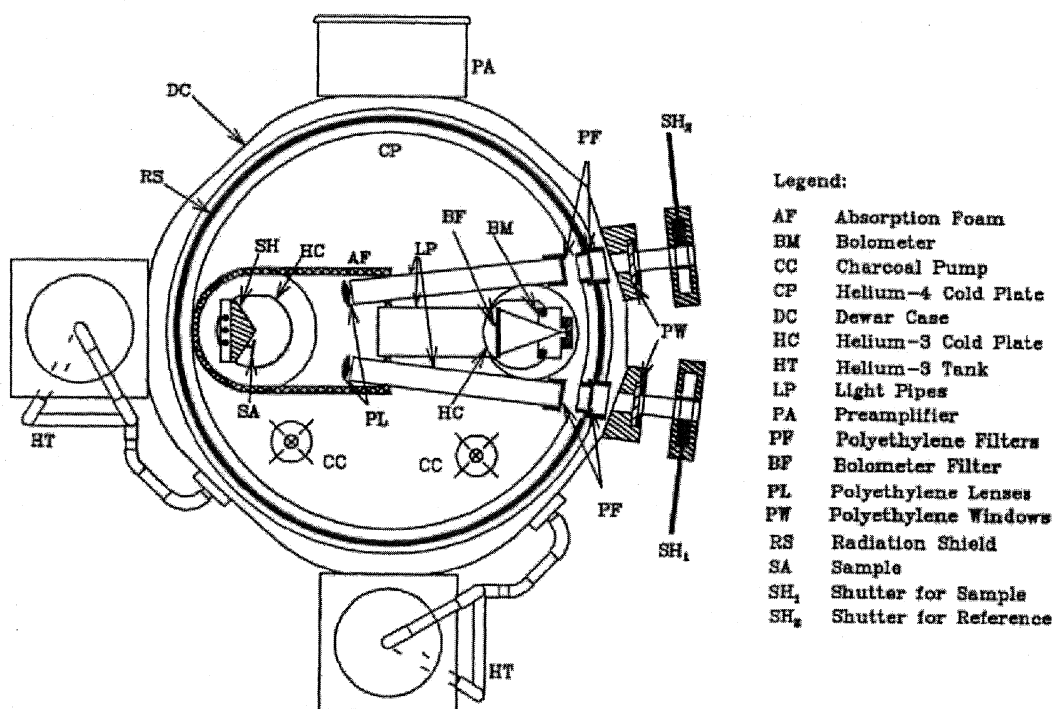
Figure 3.2: **The scheme of a ^{3}He cryostat [16]**

The cryostat is interfaced with the Martin-Puplett interferometer via a brass pipe. The light entering the cryostat can travel either to the sample or reference mirror. This is accomplished by using two electronically controlled shutters (SH1 and SH2) and a flip mirror. The beam of light may travel only through one path at a time. The light is then

reflected from the target (sample or ref. mirror) to the bolometer.

The basic problem with low temperature work is to provide suitable thermal insulation. So, before filling any dewar, it must have an adequate vacuum. In Figure 3.3 we can see a rough scheme of the ^{3}He cryostat.
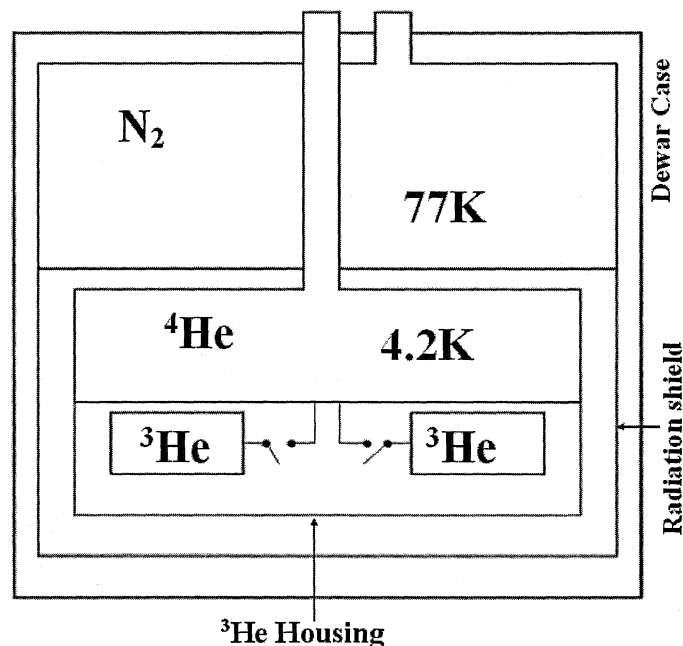
Figure 3.3: **The rough scheme of a ^{3}He cryostat**

The purpose of the empty space separating all of the vessels is to thermally insulate the cryostat from the ambient temperature, and also to insulate the liquid Nitrogen vessel from the liquid Helium vessel (^{4}He). The process of cooling the cryogenic system down is the following:

The cryostat is evacuated using a pumping system consisting of a combination of a rotary pump and a turbomolecular pump. The cryostat is pumped down for a long time period, usually 2-3 days. The low limit for the vacuum in the system is approximately 3×10^{-6} Torr (the order of 10^{-4}Pa). Then both of the containers (^{4}He and N_2 container) are filled with liquid nitrogen (T = 77 K) to pre-cool the cryogen vessels. Precooling the

cryostat is an important step, which reduces the amount of liquid ^{4}He used during the transfer. When the system is equilibriated (5-9 hours), the ^{4}He container is voided and it is filled with liquid ^{4}He (temperature 4.21K). After thermally stabilizing the cryostat (this is usually done during the night, for appr. 8 hours), the bolometer and sample stage are brought down to (1.8 - 1.9)K by pumping on the liquid ^{4}He. As can be seen in Figure 3.3 these two stages are thermally connected to another set of vessels - to the ^{3}He containers. When the whole system is being cooled down, the isotope of helium, ^{3}He, gets liquified at the temperature T = 3.19 K. After reaching the low pressure limit for the rotary pump, used for cooling down the system to T $\simeq$ 1.8K, both of the ^{3}He stages are disconnected from the ^{4}He container, and the same procedure is used to get these cryogenic stages to even lower temperatures. By use of internal charcoal pumps, the vapor pressure above the ^{3}He liquid is lowered resulting in a temperature decrease down to 0.37K. For the rest of the experiment, the temperature at the bolometer stage is kept at this value. The temperature at the sample stage can be changed by adding some heat to this stage. (In the range (0.5K - 4.2K) this can be done by changing the thermal connections to the charcoal pump and/or the ^{4}He reservoir.)

3.3 The Bolometer

Two silicon bolometers can be used for the measurements, one that operates below 0.4 K and another one, that operates below 4.2 K. The choice of the bolometer used depends on the temperature and frequency range measured during the experiment. The bolometers are of the composite type and feature a small silicon element thermally bonded to a suitably blackened 5.0 mm diameter sapphire absorber mounted in a cylindrical cavity. The entrance cone for the bolometer is gold plated to prevent tarnish, and to improve thermal properties [17].

A bolometer is an instrument for detecting and measuring radiation in amounts as

small as 10^{-13} Joule. It was invented in 1880 by Samuel P. Langley. Basically it consists

of a radiation-sensitive resistance element in one branch of a Wheatstone bridge.
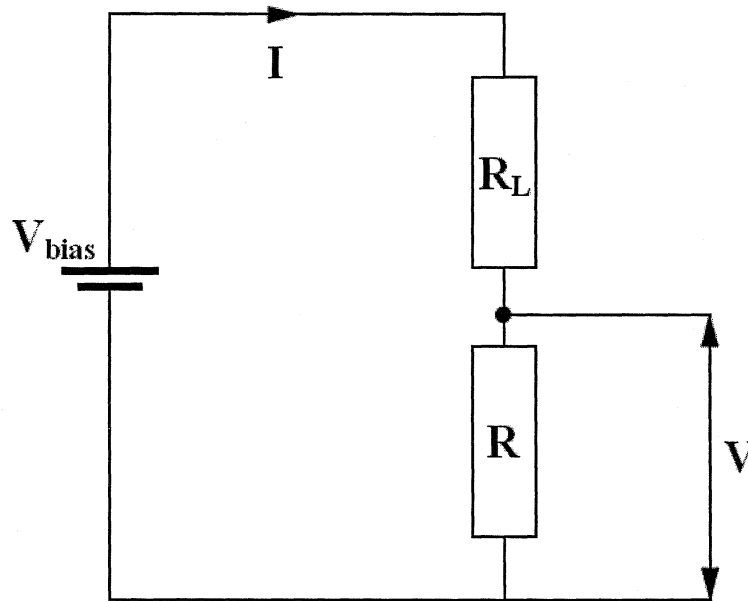
Figure 3.4: **The schematic bolometer bias circuit**

Changes in radiation incident on the sensor cause changes in the electrical resistance

of the element [18]. The temperature rise causes a change in the resistance of the bolome-

ter and consequently in the voltage across it. This change in voltage is amplified and

measured. Thus, resistance is measured before and after the application of rf power. If

the same change in resistance is then produced by a variable DC source of power, then

the rf power is equal to the measured DC power. This relationship makes possible the

direct calibration of a bridge circuit in units of power [19].

Chapter 4

Basic Electromagnetic Properties of Matter

4.1 Electrical Resistivity

Electrical resistivity is one of the key physical properties for all materials. The resistivity of different materials at room temperature can vary by over 20 orders of magnitude. The electrical resistivity of a material is a quantity describing how much that material resists the flow of electricity. If electric current can flow easily through a material, the material is said to have low resistivity.

The resistivity of a material can vary greatly with the temperature. The resistivity of metals usually increases as temperature increases, while the resistivity of semiconductors usually decreases as temperature increases, and in superconducting materials the electrical resistivity vanishes at the critical temperature T_c.

Measuring the temperature dependence of the electrical resistivity is a straightforward way to examine possible superconductivity of new materials, or to specify T_c for a given sample in order to characterize it before carrying out more complex experiments later; the latter being the main purpose of running resistivity measurements in this thesis. To understand the basic idea of electrical resistivity, let us think about the cloud of electrons in the lattice consisting of stationary positive ions.

4.1.1 Simple Model

Figure 4.1 shows a simple microscopic model of electric current flowing through a material. While this model presents a very simplified idea of the origin of resistivity, it is still
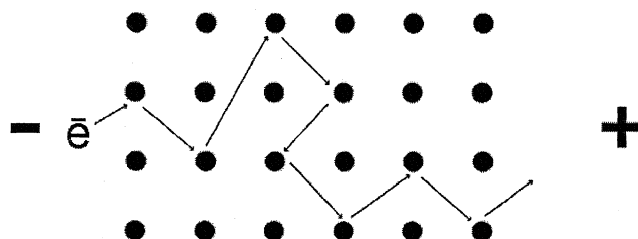
Figure 4.1: **Simple model of electric current flowing through a solid material**

a useful concept for recognizing its basics and making rough estimates of some physical properties. (A more correct approach to the electrical resistivity of materials requires a thorough understanding of quantum mechanics.) On a microscopic level, electricity is simply the movement of electrons through a material. The electron tends to move from the left side of the material to the right side because an external force acts on it. As the electron moves through the material, it collides with the stationary atoms of the material, represented by the black circles. These collisions tend to slow down the electron. The effect of the material on the motion of an electron, can then be approached by means of simple statistics, where the regularly ordered atoms absorb a part of the electron's kinetic energy, what can be described with one property of the material - its resistivity.

Thus far it was assumed, that the material being measured is homogeneous and isotropic. This is not always a valid assumption. A more exact definition of resistivity is the proportionality coefficient ρ relating a local applied electric field to the resultant current density:

$$\vec{E} \equiv \rho \vec{J} \qquad (4.1)$$

where $\vec{E}$ is the electric field (V/m), $\vec{J}$ is the current density (A/m^2), and ρ is a proportionality coefficient (Ω.m). Equation 4.1 is one form of Ohm's law. Let us consider now the case of a bar-shaped sample (Figure 4.2).
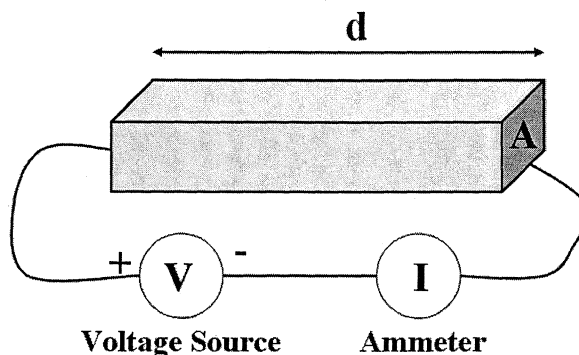
Figure 4.2: **Measuring the resistivity for a bar-shaped homogeneous sample**

The magnitude of electric field E is given by the voltage V divided by the distance d over which the voltage is applied:

$$E \equiv \frac{V}{d} \tag{4.2}$$

The current density J is given by the current I, divided by the cross-sectional area A through which the current flows:

$$J \equiv \frac{I}{A} \tag{4.3}$$

Combining equations 4.1, 4.2, and 4.3 and rearranging gives:

$$V = \frac{I\rho d}{A} \tag{4.4}$$

Now define a new quantity called resistance R with the definition:

$$R = \frac{\rho d}{A} \tag{4.5}$$

Combining equations 4.4 and 4.5 then gives:

$$I = \frac{V}{R} \tag{4.6}$$

where I is the current in amperes (A) flowing through the sample, V is the voltage in volts (V) applied across the sample, and R is the resistance in ohms (Ω) of the sample. Equation 4.6 is another form of Ohm's law. Note that the resistance R can depend on the size and shape of the sample, while ρ is independent of the size, or shape, of the sample. For example, if the length d of the sample bar is doubled, the resistance will double but the resistivity will remain constant. Thus the resistivity is a quantity that represents the resistance to the flow of current through a sample, that is independent of the sample geometry. In real experiments, it is often necessary to measure small samples with arbitrary shape. One of the methods of dealing with this situation is the van der Pauw technique for measuring the resistivity.

4.1.2 Van der Pauw Technique

This method is a general four-point resistivity measurement technique that allows measurements on samples of arbitrary shape, with no need to measure all the physical dimensions of the sample. There are four conditions that must be satisfied to use this technique [20]:

a) The sample must have a flat shape of uniform thickness.

b) The sample must not have any isolated holes.

c) The sample must be homogeneous and isotropic.

d) All four contacts must be located at the edges of the sample.

In addition to these four conditions, the area of contact of any individual contact should be at least an order of magnitude smaller than the area of the entire sample. For small samples, this might not be possible or practical. If sufficiently small contacts are not achievable, it is still possible to do accurate van der Pauw resistivity measurements, using geometric correction factors to account for the finite size of the contacts.

The illustration of Figure 4.3 shows one possible sample measurement geometry.
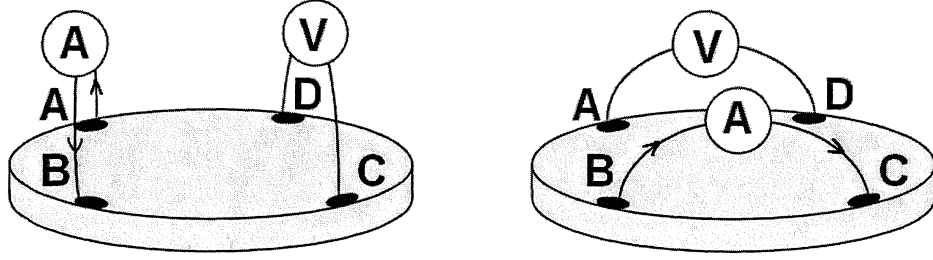
Figure 4.3: **Method of van der Pauw**

The procedure for doing a van der Pauw measurement is as follows. We consider a flat sample of a conducting material of arbitrary shape with successive contacts A, B, C and D fixed on arbitrary places along the circumference such that the above-mentioned conditions (a) to (d) are fulfilled. We define the resistance $R_{AB,CD}$ as the potential difference $V_D - V_C$ between the contacts D and C per unit current through the contacts A and B. The current enters the sample through A and leaves through the contact B. Similarly we define the resistance $R_{BC,DA}$. It can be shown [20], that the following relation holds

$$e^{-\pi R_{AB,CD}d/\rho} + e^{-\pi R_{BC,DA}d/\rho} = 1 \qquad (4.7)$$

where ρ is the resistivity of the material and d is the thickness of the sample. Equation 4.7 determines uniquely the value of ρ as a function of $R_{AB,CD}$, $R_{BC,DA}$ and d. In order to facilitate the solution of ρ from equation 4.7, we write it in the form

$$\rho = \frac{\pi d}{\ln 2} \frac{(R_{AB,CD} + R_{BC,DA})}{2} f\left(\frac{R_{AB,CD}}{R_{BC,DA}}\right) \qquad (4.8)$$

where f is only function of the ratio $R_{AB,CD}/R_{BC,DA}$. If $R_{AB,CD}$ and $R_{BC,DA}$ are almost equal, f can be approximated by the formula

$$f \approx 1 - \left(\frac{R_{AB,CD} - R_{BC,DA}}{R_{AB,CD} + R_{BC,DA}}\right)^2 \frac{\ln 2}{2} - \left(\frac{R_{AB,CD} - R_{BC,DA}}{R_{AB,CD} + R_{BC,DA}}\right)^4 \left\{\frac{(\ln 2)^2}{4} - \frac{(\ln 2)^3}{12}\right\} \qquad (4.9)$$

More details about the van der Pauw technique can be found in [20].

4.2 Magnetic Susceptibility

Just as a dielectric contains electric dipoles that contribute to the field, so there are magnetic media that contain magnetic dipoles [21]. Depending on the response of these dipoles to the external magnetic field, we divide the materials into three groups: diamagnetic, paramagnetic and ferromagnetic. Generally speaking - the diamagnetic materials decrease the field penetrating into them and paramagnetic materials amplify the magnetic field entering them. Ferromagnetic materials can be considered as an extreme case of paramagnetic materials with a very strong response to the magnetic field [21]. In a magnetic medium, where there are magnetic dipoles distributed through the volume of the material, we define the magnetization vector M as the vector sum of the dipole moments in unit volume, so the magnetization M of a dielectric is defined by

$$M = Nm \tag{4.10}$$

where N is the number of magnetic dipoles per unit volume and m is the magnetic dipole moment per dipole.

The magnetic field inside a material is given by [21]

$$B = \mu_0(H + M) \tag{4.11}$$

where H is the external magnetic field intensity.

In the diamagnetic or paramagnetic medium, the magnetization M is proportional to B [21]. Thus both these vectors are proportional to H and one may write

$$B = \mu H = \mu_{rel}\mu_0 H \tag{4.12}$$

where the dimensionless quantity μ_{rel} is generally referred to as the relative permeability.

The ratio of magnetization M to magnetic field intensity H is called the magnetic susceptibility and is defined as

$$M = \chi_m H \tag{4.13}$$

Thus, the magnetic susceptibility is a measure of the ability of a material to be magnetized. It is an important property of materials. On the surface it describes how a material will interact with an applied magnetic field. The proportionality constant links magnetization to the applied magnetic field intensity (at levels below which saturation and hysteresis are important). Magnetic susceptibility, χ_m, is then related to magnetic permeability μ by

$$\mu = \mu_0(1 + \chi_m). \tag{4.14}$$

Rearranging the equation 4.13 we have

$$\chi_m = \frac{M}{H}, \tag{4.15}$$

which can be directly used in magnetic experiments.

4.2.1 Measuring the AC Susceptibility

AC magnetic susceptibility is an important tool for investigating magnetic and superconducting materials [22]. The AC susceptibility of a sample is defined in accordance with 4.15 as

$$\chi_m = \frac{\partial M}{\partial H} \tag{4.16}$$

The measurement of the AC susceptibility offers a non-invasive technique capable of confirming, if there is a superconducting transition occurring in the sample.

In our experimental setup the AC susceptibility measures a change in mutual inductance of a primary and two identical (but oppositely wound) secondary coils when a sample is inserted into the inner space of the primary and one of the secondary coils, which have a common axis (see Figure 4.4). The two secondary coils are connected in series so that the output is nearly balanced without the presence of a sample [22]. The sample is placed on a sample holder (Sapphire rod) and mounted on the bolometer
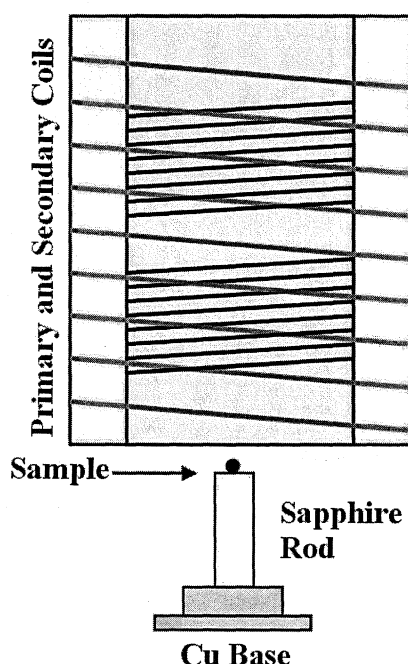
Figure 4.4: **Scheme of the experimental set-up for susceptibility measurements**

stage of the ^{3}He cryostat together with the coils, so that temperature dependant measurements can be carried out. More details about the experimental setup for the AC magnetic susceptibility can be found in reference [22].

4.3 Resistivity and Susceptibility Measurements in a Superconducting State

To carry out measurements of the electrical resistivity and/or magnetic susceptibility is a straightforward way of examining possible superconducting transition in a solid matter. Both techniques described in the sections 4.1.2 and 4.2.1 were used in this thesis work as preliminary experiments to characterize the superconducting properties of the samples of heavy-fermion superconductor CeCoIn$_5$ utilized for optical spectroscopy measurements. The results of these measurements can be found in chapter 6.

Chapter 5

Heavy Fermion Systems

5.1 Introduction to Heavy Fermions

Heavy fermion systems are inter-metallic compounds that exhibit very unusual low temperature properties. One of their constituents is a member of the lanthanide (Ce, Yb) or actinide (U) group of the periodic table (See Figure 5.1). The unifying characteristic behind all heavy-fermion systems is a large, low temperature density of electronic states at Fermi level. This large density of states is interpreted as an enhancement of the mass of the conduction electrons due to their interaction with the spin of electrons in the unfilled f-band of the magnetic rare-earth ions [23]. Their effective masses can reach hundreds or even a thousand times the mass of a free electron as a consequence of this interaction; hence the name heavy fermions or heavy electrons. At room temperature and above, heavy electron systems behave as a weakly interacting collection of f-electron moments with ordinary masses. As the temperature is lowered the f-electron moments become strongly coupled to the conduction electrons and to one another, and the conduction electron effective mass is typically several orders of magnitude larger than the bare electron mass.

Despite the common characteristic of having a large value for the electronic effective mass at low temperatures, heavy-electron systems display a variety of ground states. The four main groups are: Non-magnetic, coherent Fermi-liquids (e.g. $CeAl_3$, UPt_4Au), magnetic (e.g. UCu_5, $CePb_3$) and superconducting (e.g. UBe_{13}, UPd_2Al_3) [24]. The latter

The Periodic Table of Elements

Atomic Number = Number of Protons = Number of Electrons

6 → C ← Chemical Symbol

CARBON ← Chemical Name

12 ← Atomic Weight = Number of Protons + Number of Neutrons

NON-METALS

METALS

1 H HYDROGEN 1																	2 He HELIUM 4
3 Li LITHIUM 7	4 Be BERYLLIUM 9											5 B BORON 11	6 C CARBON 12	7 N NITROGEN 14	8 O OXYGEN 16	9 F FLUORINE 19	10 Ne NEON 20
11 Na SODIUM 23	12 Mg MAGNESIUM 24											13 Al ALUMINUM 27	14 Si SILICON 28	15 P PHOSPHORUS 31	16 S SULFUR 32	17 Cl CHLORINE 35	18 Ar ARGON 40
19 K POTASSIUM 39	20 Ca CALCIUM 40	21 Sc SCANDIUM 45	22 Ti TITANIUM 48	23 V VANADIUM 51	24 Cr CHROMIUM 52	25 Mn MANGANESE 55	26 Fe IRON 56	27 Co COBALT 59	28 Ni NICKEL 59	29 Cu COPPER 64	30 Zn ZINC 65	31 Ga GALLIUM 70	32 Ge GERMANIUM 73	33 As ARSENIC 75	34 Se SELENIUM 79	35 Br BROMINE 80	36 Kr KRYPTON 84
37 Rb RUBIDIUM 85	38 Sr STRONTIUM 88	39 Y YTTRIUM 89	40 Zr ZIRCONIUM 91	41 Nb NIOBIUM 93	42 Mo MOLYBDENUM 96	43 Tc TECHNETIUM 98	44 Ru RUTHENIUM 101	45 Rh RHODIUM 103	46 Pd PALLADIUM 106	47 Ag SILVER 108	48 Cd CADMIUM 112	49 In INDIUM 115	50 Sn TIN 119	51 Sb ANTIMONY 122	52 Te TELLURIUM 128	53 I IODINE 127	54 Xe XENON 131
55 Cs CESIUM 133	56 Ba BARIUM 137		72 Hf HAFNIUM 178	73 Ta TANTALUM 181	74 W TUNGSTEN 184	75 Re RHENIUM 186	76 Os OSMIUM 190	77 Ir IRIDIUM 192	78 Pt PLATINUM 195	79 Au GOLD 197	80 Hg MERCURY 201	81 Tl THALLIUM 204	82 Pb LEAD 207	83 Bi BISMUTH 209	84 Po POLONIUM 209	85 At ASTATINE 210	86 Rn RADON 222
87 Fr FRANCIUM 223	88 Ra RADIUM 226		104 Rf RUTHERFORDIUM 263	105 Db DUBNIUM 262	106 Sg SEABORGIUM 266	107 Bh BOHRIUM 264	108 Hs HASSIUM 277	109 Mt MEITNERIUM 268	110 Uun UNUNNILIUM 281	111 Uuu UNUNUNIUM 272	112 Uub UNUNBIUM 285	113 Uut UNUNTRIUM NOT YET OBSERVED	114 Uuq UNUNQUADIUM 289	115 Uup UNUNPENTIUM NOT YET OBSERVED	116 Uuh UNUNHEXIUM NOT YET OBSERVED	117 Uus UNUNSEPTIUM NOT YET OBSERVED	118 Uuo UNUNOCTIUM NOT YET OBSERVED

KEY

☐ = Solid at room temperature
● = Liquid at room temperature
☁ = Gas at room temperature
☢ = Radioactive
♀ = Artificially Made

57 La LANTHANUM 139	58 Ce CERIUM 140	59 Pr PRASEODYMIUM 141	60 Nd NEODYMIUM 144	61 Pm PROMETHIUM 145	62 Sm SAMARIUM 150	63 Eu EUROPIUM 152	64 Gd GADOLINIUM 157	65 Tb TERBIUM 159	66 Dy DYSPROSIUM 163	67 Ho HOLMIUM 165	68 Er ERBIUM 167	69 Tm THULIUM 169	70 Yb YTTERBIUM 173	71 Lu LUTETIUM 175
89 Ac ACTINIUM 227	90 Th THORIUM 232	91 Pa PROTACTINIUM 231	92 U URANIUM 238	93 Np NEPTUNIUM 237	94 Pu PLUTONIUM 244	95 Am AMERICIUM 243	96 Cm CURIUM 247	97 Bk BERKELIUM 247	98 Cf CALIFORNIUM 251	99 Es EINSTEINIUM 252	100 Fm FERMIUM 257	101 Md MENDELEVIUM 258	102 No NOBELIUM 259	103 Lr LAWRENCIUM 262

Figure 5.1: The Periodic Table of Elements [25]

being a surprising result given that in ordinary superconductors a dilute concentration of magnetic impurities destroys superconductivity [26].

Some unique features of the low temperature normal state properties of heavy electron systems are:

1) A very large specific heat. For example, the inter-metallic $CeAl_3$, the first known heavy-electron system [27], has a gamma coefficient of 1620 mJ/mol.K^2, one of the largest for all such compounds. As the temperature goes to zero, we can write the specific heat C(T) in form

$$\frac{C(T)}{T} = \gamma + BT^2 \qquad (5.1)$$

where γ is the specific heat coefficient and B characterizes the contribution of the phonons to the specific heat. In heavy fermion systems γ is so large, that the BT^2 term can be ignored (at least up to approximately 20 K). Since deviations from a linear electronic specific heat occur, one often writes

$$\frac{C(T)}{T} = \gamma(T). \qquad (5.2)$$

Several values for the specific heat coefficient are listed in Table 5.1 and compared to the values of conventional metals.

A popular way of probing the electron effective mass is by determining the density of states at the Fermi level. This is often done by measuring the electronic specific heat of a system, C, which at very low temperatures ($< 1K$) is proportional to the density of states at the Fermi energy, and therefore, to the electron effective mass, m*. Normal metals like Cu or Au have values for gamma of the order of 1 mJ/mol.K^2 and transition and rare earth metals have values ten times as large, while heavy-fermion systems show values in the hundreds (in some cases the thousands) of mJ/mol.K^2.

2) A transport property that characterizes metals is a low resistivity. The heavy fermion (HF) systems have room temperature values that are enhanced over that of conventional metals, but not by so much that the systems are not still metals. Typical values

Type of Material	Room Temp. Resistivity ρ [$\mu\Omega$cm]	T^2 - Coefficient of Resistivity A [$\mu\Omega$cm/K^2]	Specific Heat Coefficient $\gamma(0)$ [mJ/mol.K^2]
HF Superconductor UPt$_3$	150	3	450
HF Magnet U$_2$Zn$_{17}$	110	negligible	400
Normal HF CeAl$_3$	170	35	1620
Conventional Metal Pd	20	10^{-5}	9.4
Conventional Metal Ag	2	10^{-7}	0.6

Table 5.1: **Comparison of heavy fermions and normal metals [23]**

of the resistivity are compared with conventional metals in Table 5.1. As the temperature decreases from room temperature the resistivity of a heavy fermion metal typically increases while that for a conventional metal decreases. Nonetheless at a sufficiently low temperature the resistivity of the heavy fermion system turns downward and for very low temperature in many cases has a T^2 dependence, i.e.

$$\rho(T) = \rho(0) + AT^2 \tag{5.3}$$

The second column of Table 5.1. shows the enormous enhancement of the A coefficient over that of conventional metals. The temperature dependence of the resistivity of several heavy fermion compounds displaying a range of behaviors is given in Figure 5.2. The intermediate temperature regime (10 K < T < 300 K) is characterized by unusual structure in the thermodynamic and transport properties. For example a peak in the resistivity is observed in most heavy fermion systems [26]. (UPt$_3$ being one of the exceptions; note that the resistivities at room temperature have been normalized to the same value.)
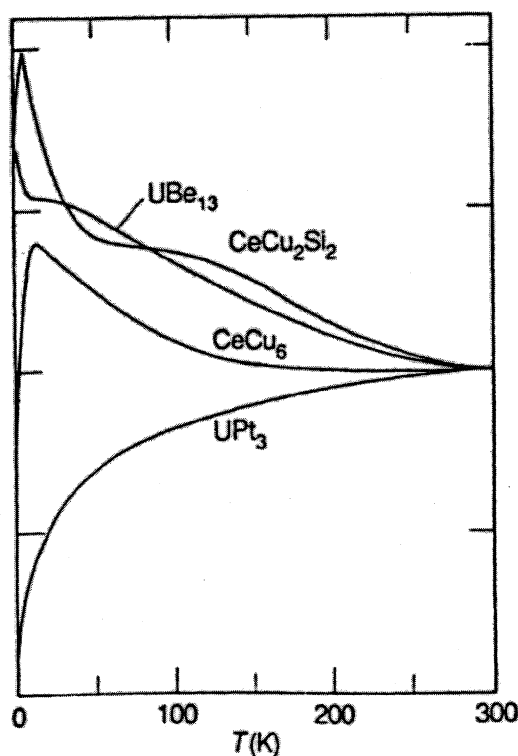
Figure 5.2: **Resistivity vs. temperature for several heavy-electron metals [26]**

5.2 Heavy Fermion Superconductors

Heavy-fermion superconductors are materials in which superconductivity[1] emerges out

of a normal state with strong electronic correlations [28]. Of the vast number of metallic

compounds, only a small fraction enters a superconducting state at low temperatures, and

of this small number, an even smaller fraction develops superconductivity out of a normal

---

[1]A phenomenon when the electrical resistivity of a material drops to zero. At a critical temperature

T_c the specimen undergoes a phase transition from a state of normal electrical resistivity to a super-

conducting state. A bulk superconductor in a weak magnetic field will act as a perfect diamagnet with

zero magnetic induction in the interior. The superconducting state is an ordered state of the conduc-

tion electrons of the metal. The order is in the formation of loosely associated pairs of electrons. The

electrons are ordered at temperatures below the transition temperature and they are disordered above

the transition temperature.

state in which electronic correlations produce orders-of-magnitude enhancement of the conduction electron effective mass. This subset of materials, known as heavy-fermion superconductors, has been an influential area of research in condensed-matter physics since its first member $CeCu_2Si_2$ was discovered in 1979 [29]. In spite of progress, the heavy-fermion problem and heavy-fermion superconductivity in particular remain a challenge to experiment and theory. Though heavy-fermion behavior has been found in several structure types, it appears that, like conventional BCS superconductivity, heavy-fermion superconductivity may be favored by particular crystallographic structures [28, 30]. Because of the limited number of examples, very little is known about relationships that might exist between the structure and properties of these materials. Any predictive understanding of how superconductivity can emerge in the highly correlated ground state has to be able to explain why it appears in one crystal structure and not another. This makes the discovery of a new prototype structure (like $CeMIn_5$) for heavy-fermion superconductivity of special interest [30].

The interaction of magnetism and superconductivity is a significant and long standing problem in condensed matter physics. Usually, the presence of magnetic order undermines superconductivity, but in heavy fermion materials, superconductivity and magnetism can coexist without deleterious consequences to the superconducting state. These systems provide an opportunity to explore the interaction of magnetic and superconducting order parameters as a function of temperature, pressure, or magnetic field [31].

In a conventional superconductor, the binding of electrons into the paired states that collectively carry the supercurrent is mediated by phonons, which are vibrations of the crystal lattice [32]. The existence of magnetically mediated superconductivity in some compounds could help shed light on the question of whether magnetic interactions are relevant for describing the superconducting and normal-state properties of other strongly correlated electron systems, perhaps including the high-temperature cop-

per oxide superconductors [32]. Recent analyses of the features of strongly correlated superconductors present the magnetic interactions as being decisive in the mechanisms for obtaining several kinds of fermionic coupling that generates superconductivity in a variety of compounds. The transition to the superconducting state in these materials seems to be caused by certain fluctuating magnetic waves that can be propagated either in non-ordered systems or in materials that present ferromagnetic or anti-ferromagnetic ordering [33]. It seems that, although there is no clear mechanism which fully satisfies all the characteristic behavior of this superconductivity, phonons can be ruled out as being responsible for the pairing. In these systems, the superfluid state seems to be parasitic of its authentic phase transition that can be anti-ferromagnetic or even ferromagnetic and whose energy interval is larger than that in which superconductivity occurs [33]. In addition, the unusual temperature dependence of the specific heat for temperatures less than T_c is a clear feature of unconventional superconductivity, which suggests node lines in the superconducting gap, possible with an anisotropic pair potential arising from magnetic interactions. As is well known, the main behaviors of these heavy-fermion materials are governed by the concurrence of band effects, hybridization of localized f states with extended states, exchange interaction between these states, and Heisenberg interaction between the localized spins [33].

The presence of a strong magnetic interaction between 4f moments and itinerant electrons in this class of compounds allows the possibility of non-phonon mediated coupling between superconducting quasi-particles (a signature of unconventional superconductivity) and a superconducting order parameter with lower symmetry than that of the underlying crystal lattice.

Soon after the discovery of superconductivity in $CeCu_2Si_2$ [29], several uranium-based heavy fermion superconductors were discovered. The presence of a double transition in UPt_3 immediately identified this compound as an unconventional superconductor [34].

Subsequent observations of power law temperature dependences of the specific heat and thermal conductivity have been instrumental in identifying UPt_3 (and other U-based heavy fermion superconductors) as unconventional [34]. Until very recently, among Ce-based heavy fermion compounds only $CeCu_2Si_2$ was shown to superconduct at ambient pressure. Other Ce-based compounds with the $ThCr_2Si_2$ structure require application of significant pressure (on the order of 20 kbars) before they exhibit superconductivity. These include $CeCu_2Ge_2$, $CePd_2Si_2$, and $CeRh_2Si_2$ [34].

Recently, cubic $CeIn_3$ was shown to superconduct under pressure of about 25 kbar, with superconductivity mediated by magnetic interactions [35]. Heavy-fermion $CeIn_3$ is also involved in a new recently discovered class of HF superconductors, $CeMIn_5$, the structure of which includes $CeIn_3$. In this new family $CeMIn_5$ M can be Ir, Co or Rh. One of its members - $CeCoIn_5$ - is the material examined in this thesis. An overview of existing literature about the $CeMIn_5$ compounds can be found in the following section.

5.3 Heavy Electron Metal $CeCoIn_5$

5.3.1 An Overview of $CeMIn_5$ Family

Heavy fermion metal $CeCoIn_5$ belongs to a recently discovered family of heavy fermions with chemical composition $CeMIn_5$, where M = Ir, Co or Rh. The presence of an appropriate magnetic ion - in this case Ce - enhances the effective mass m^* of conduction electrons by several orders of magnitude, thus creating one of the typical features of heavy fermion metals. These compounds have attracted much interest in recent years due to their similarity with cuprates: a quasi-two-dimensional (2D) structure and the proximity of magnetic order [36, 33, 28, 37]. The ground state of these materials depends strongly on the transition metal M, being anti-ferromagnetic for Rh, but superconducting for Ir and Co. Alloying the different members of this family produces a rich phase diagram of

superconducting and antiferromagnetic regions that can coexist with each other [38].

A question which is still open is the nature of the pairing interaction. The close association between antiferromagnetic order and superconductivity in heavy fermion systems suggests that magnetic excitations may play an important role in pairing the electrons [38]. Recent model calculations for magnetically mediated superconductivity show that this really could be a possible answer and while the origin of superconductivity in heavy-fermion materials is still unknown, there is growing evidence that it is magnetically mediated. This seems to be the case as well in the $CeM\mathrm{In}_5$ family [28]. A number of experiments on this recently discovered family of heavy fermion superconductors CeRhIn_5, CeIrIn_5 and CeCoIn_5 point to the existence of a non-Fermi-liquid (NFL) metallic state in these compounds. Similar behavior is observed in other heavy-fermion materials and is understood in terms of magnetic fluctuations near a zero-temperature critical point, where theory predicts either $\gamma \sim -ln(T)$ or $\gamma = \gamma_0 - AT^{1/2}$ depending on the dimensionality and nature of the magnetism [37].

Let us note here, that typical of a Landau Fermi liquid are that C/T and χ are constant as $T \rightarrow 0K$ and that the resistivity behaves as $\rho = \rho_0 + AT^2$, independent of the strength of electron-electron interactions as long as the concept of a quasiparticle remains valid.

As an example from the $CeM\mathrm{In}_5$ family - there is a transition in CeIrIn_5 to a zero-resistance state at 1.2 K that is significantly above the bulk T_c, as determined by specific heat and susceptibility, and the resistivity varies as $\rho = \rho_0 + AT^{1.3}$ up to 5 K (and down to 0.06 K in a magnetic field sufficient to suppress superconductivity). This non-Fermi-liquid (NFL)-like temperature dependence of the resistivity suggests that superconductivity in CeIrIn_5 develops near or at a quantum critical point (*see next paragraph*), with associated spin fluctuations that are conducive to magnetically mediated Cooper pairing [39].

When the symmetry of the ground state of a system changes as a function of an

external or internal parameter, the system is said to undergo a quantum phase transition. If, in addition, this transition is second order, the system has a quantum critical point (QCP) at the critical value of the parameter. The competition between the nearly degenerate ground states determines the behavior of the system over a range of temperatures and tuning parameter values in the vicinity of the QCP. In this region of the phase diagram the properties of the system differ from those on either side of the transition and often exhibit unusual dependence on the temperature and the tuning parameter. This has made quantum critical phenomena a subject of intense current interest [54].

The study of quantum critical points in heavy fermion systems has been the focus of particular attention. In these materials the competition typically takes place between a paramagnetic and a magnetically ordered ground state. The unconventional behavior near a QCP is manifested in the deviation of the temperature dependence of measured properties from those of metals described by the Landau Fermi liquid (FL) theory. (The electronic specific heat is linear in temperature, $C(T) = \gamma T$, and the resistivity increases quadratically from a residual value, $\rho = \rho_0 + AT^2$.) In systems tuned to a QCP, the Sommerfeld coefficient $\gamma(T) = C/T$ commonly diverges as the temperature goes to zero and has been variously argued to behave as either $logT$ or T^α, with $\alpha < 0$. A resistivity with an exponent less than 2 is also ubiquitous in these compounds [54].

Tuning the system through a QCP can be accomplished experimentally by varying the sample's composition, applying pressure, or applying a magnetic field. In nonstoichiometric compounds the Kondo disorder is an important mechanism leading to a non-Fermi liquid (NFL) behavior. In these compounds it is not easy to separate this origin of NFL behavior from the consequences of the proximity to a QCP. Hence the stoichiometric compounds receive more attention in the field of quantum criticality. One class of such materials is the Ce-based compounds [54].

The superconductivity (SC) in the CeMIn$_5$ (M = Co, Rh, Ir) heavy fermion com-

pounds provides valuable information about superconductivity in the vicinity of a possible QCP due to the excellent tunability of their superconducting properties with pressure and magnetic fields. Besides a complicated phase diagram due to a competition/interplay between magnetism and superconductivity, the superconducting properties as well as the normal state ones around the QCP exhibit various anomalous behaviors such as NFL power law dependence on temperature of the resistivity, pseudogap behavior above the superconducting critical temperature, a continuous evolution from a second order to a first order superconducting phase transition with magnetic field, etc... [40].

These materials provide the opportunity to study superconductivity in the vicinity of a magnetic instability and help expand our understanding of magnetically mediated superconductivity and its relevance to other strongly correlated electron systems. Evidence for unconventional superconductivity in these Cerium based heavy fermion superconductors is mounting. Recent heat capacity experiments, thermal conductivity measurements, and NMR relaxation rates reveal power law temperature dependences at low temperatures. This has been interpreted as an indication of an unconventional superconductivity with line nodes [41].

These materials are often compared to cuprates (copper oxides). While cuprate superconductors were discovered almost two decades ago, a microscopic theory to explain their high T_c and anomalous normal state properties is still an area of ongoing research. It has been suggested that the anomalous normal state properties arise from the proximity to a quantum phase transition associated with the onset of spin density wave (SDW) or charge density wave (CDW) ordering in a Fermi liquid and that at optimal (or near optimal) doping a quantum critical point occurs. The crossover from the pseudogap state at underdoping to the Fermi liquid state in the overdoped regime is a consequence of the model [55].

Though the issue of quantum criticality and superconductivity came to prominence in

the context of cuprates, there have been several recent examples of this interplay in heavy fermion compounds. Like the cuprates, unconventional superconductivity in Ce-based heavy fermions develops out of a distinctly NFL normal state that evolves in proximity to a continuous $T = 0$ antiferromagnetic transition, but (unlike the cuprates) this state can be accessed cleanly by applied hydrostatic pressure and without introducing extrinsic disorder associated with chemical substitutions. In addition to chemical inhomogeneity in the cuprates, a further "complication" is the existence of a pseudogap state above T_c for dopings less than optimal [53].

Characteristic of heavy-fermion systems, each member exhibits a large Sommerfeld coefficient γ (equal to C/T as $T \rightarrow 0$) in the specific heat C. CeIrIn$_5$ and CeCoIn$_5$ are bulk superconductors with transition temperatures at $T_c = 0.4$ and 2.3 K and normal-state values of $\gamma \sim = 750$ mJ/(mol.K^2) and 1200 mJ/(mol.K^2), respectively. CeRhIn$_5$ displays heavy-fermion antiferromagnetism with $T_N = 3.8$ K at ambient pressure, but applied pressure of order 16 kbar can induce an apparently first-order transition from the magnetically ordered state to a superconducting one with $T_c = 2.1$ K [42]. A precise value of its γ is difficult to establish unambiguously because of the Néel order, but a lower limit of approximately 400 mJ/(mol.K^2) has been set [39].

The temperature that CeCoIn$_5$ was observed to superconduct at ($T_c = 2.3$ K), is the highest T_c yet reported for a heavy fermion superconductor [28, 31, 33].

5.3.2   Crystal Structure of CeMIn$_5$

The crystal structure of the heavy-fermion metals CeMIn$_5$ is a tetragonal lattice of the HoCoGa$_5$ type, space group P4/mm [28, 43, 33]. One way to view these materials is as a composite of alternating CeIn$_3$ and MIn$_2$ layers, where CeIn$_3$ is itself a 3-D heavy fermion superconductor ($T_c = 200$ mK at 25 kbar) [38, 31]. The crystal structure of the CeMIn$_5$ family can be seen in Figure 5.3.
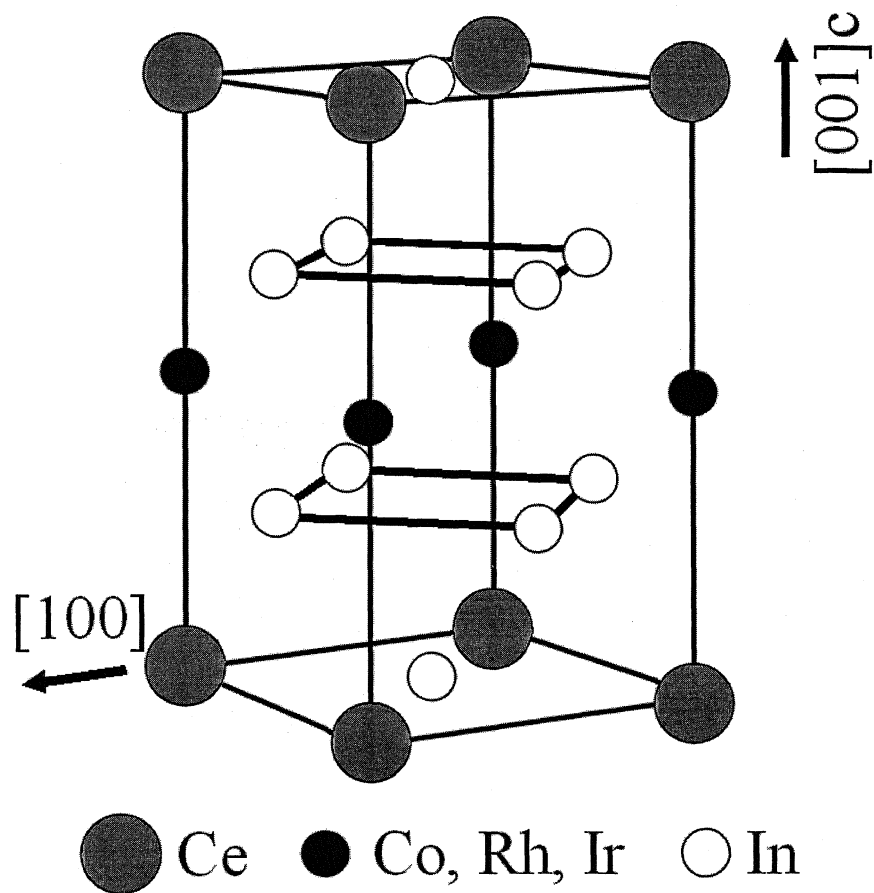
Figure 5.3: The crystal structure of CeMIn$_5$ compounds [44]

The lattice constants for all of the CeMIn$_5$ compounds can be found in table 5.2. The structural model of CeCoIn$_5$ has the following atomic coordinates: Ce at (0, 0, 0), Co at (0, 0, 1/2), In1 at (1/2, 1/2, 0) and In2 at (0, 1/2, z = 0.3094). The 3rd row in table 5.2 is the positional parameter z (or zIn2) defined with respect to the lattice parameter c. The 4th and 5th rows in the table represent the interatomic distances between the Cerium and the Indium atoms in the ab-plane, and the Cerium and the Indium atoms out of the ab-plane, respectively. The last row in the table shows the interatomic distance between the transition metal M and an Indium atom.

	CeIn$_3$	CeCoIn$_5$	CeRhIn$_5$	CeIrIn$_5$
a [Å]	4.689	4.61292	4.656	4.674
c [Å]		7.5513	7.542	7.501
zIn$_2$		0.3094	0.3053	0.3052
Ce-In1 [Å] ($\times 4$)	3.3156	3.26183	3.292	3.3050
Ce-In2 [Å] ($\times 8$)		3.283	3.2775	3.272
M-In [Å] ($\times 8$)		2.7187	2.7500	2.7560

Table 5.2: **Lattice constants for CeMIn$_5$ family [43]**

5.3.3 Growth of CeCoIn$_5$

Single crystals of CeCoIn$_5$ were grown using an Indium flux method in the group of Dr. Razavi at Brock University.

Heavy fermion CeCoIn$_5$ was synthesized by combining stoichiometric amounts of Ce and Co with excess of Indium in an alumina crucible and encapsulating the crucible in an evacuated quartz ampoule. Because of the deep eutectic formed between Ce and Co and the strong phase stability of CeIn$_3$, growth of CeCoIn$_5$ appears to be optimized

in dilute melts with a two-stage cooling process - an initial rapid cooling from 1220°C, where the molten material is homogenized, to 750°C and then a slower cool to 300°C. The resultant crystals are well-separated, faceted platelets with characteristic dimensions $2mm \times 1mm \times 0.1$ mm. The as-grown crystals have smooth, shiny surfaces. Crystals were separated by heating the contents of the crucible to the melting point of In and then extracting individual crystals from the melt using a small soldering iron and tweezers. Excess In was removed from the crystal surfaces using an $H_2O:HF:H_2O_2$ 4:1:1 etch. Crystals after etching exhibited silvery, flat mirror-like surfaces and no polishing was required for the later optical measurements. The method of the growth is very similar to that reported by other authors [39, 28, 38, 30, 37, 45].

Chapter 6

Results and Discussions

6.1 The Measurements of Electrical Resistivity

The initial software and hardware equipment for the resistivity measurements using the van der Pauw method were developed by M. Hildebrand, and details about the system can be found in his MSc. thesis [12]. Further software development was carried out by M. Janzen.

The van der Pauw technique was used to examine the superconducting transition of the sample - the heavy-fermion material $CeCoIn_5$, and to find the value of the transition temperature T_c.

A clean sample of $CeCoIn_5$ with dimensions $\sim 2mm \times 1mm \times 0.1mm$ was mounted on a glass plate with GE varnish (See Figure 6.1). The four contacts were made using silver
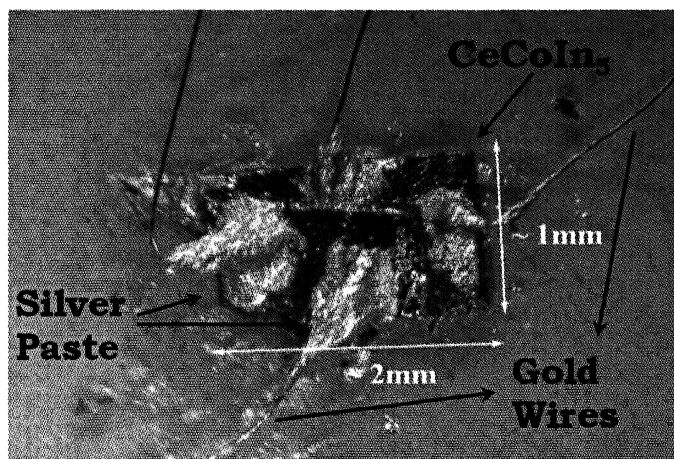
Figure 6.1: **The sample of $CeCoIn_5$ for van der Pauw resistivity measurement**

paste. Gold wire of thickness 50 μm was used to make connections to the probe. The sample was then placed into a ^{3}He cryostat and the temperature was lowered down to 0.5 K. After stabilizing ($\sim$ 30 minutes) the temperature was slowly increased by means of a heat transfer from the ^{4}He container up to 4.2 K. When all of the liquid ^{4}He was evaporated, the cryostat was left to slowly heat up through the thermal contact with the environment. This kind of experiment lasts approximately 2 days. The resulting resistivity vs. temperature dependence can be seen in Figure 6.2. As we can see in
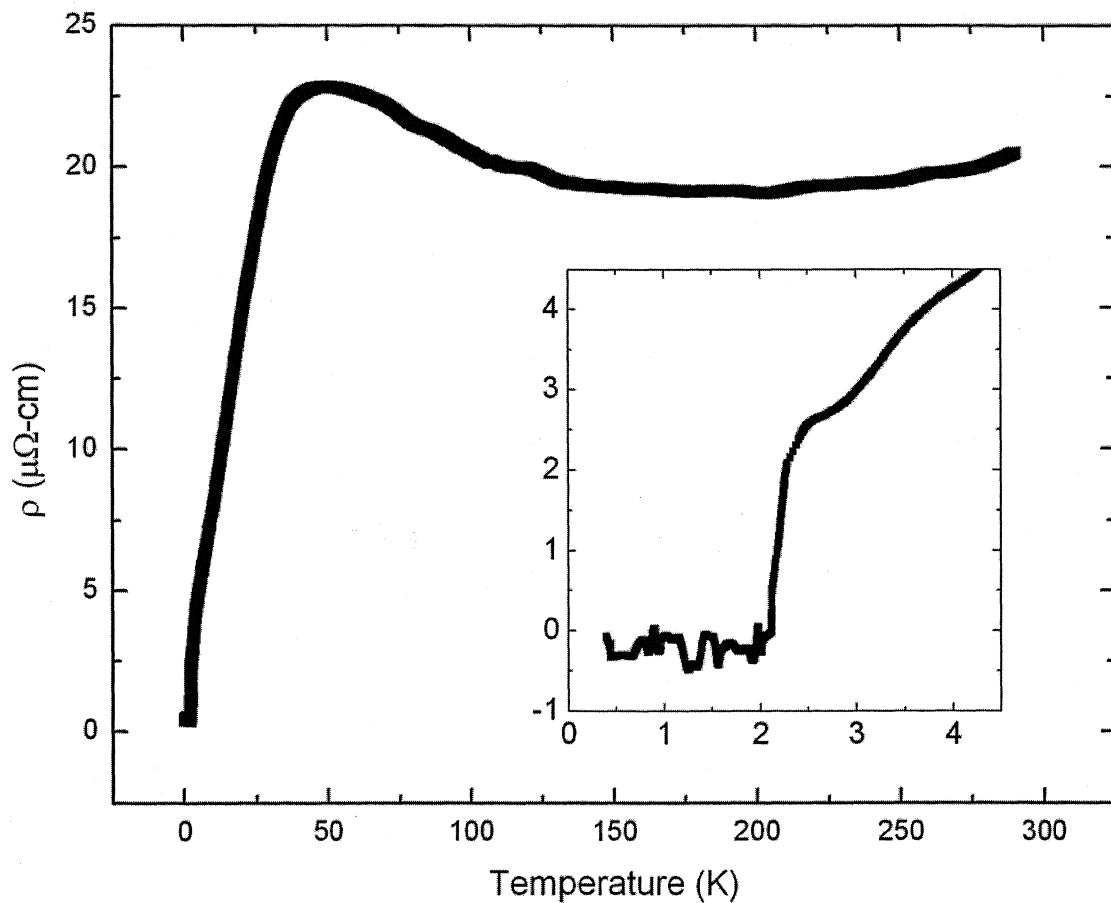
Figure 6.2: **The ab-plane resistivity of the CeCoIn$_5$**

the inset of Figure 6.2 in the range of low temperatures there is a sudden decrease in the resistivity of the sample. (Below T $\sim$ 2 K the resistivity of the sample drops to

an undetectable level and what we see in the inset of Figure 6.2 is the thermodynamic resistivity noise in the circuitry used.) The superconducting temperature $T_c \sim 2.3$ K, which is in a very good agreement with the literature [28, 30, 41].

The resistivity of CeCoIn$_5$ displays typical heavy fermion metallic behavior with a broad maximum in the resistivity close to ~ 50 K, followed by a rapid decrease at lower temperature. This behavior is generally attributed to a crossover from strong, incoherent scattering of electrons at high temperature to the development of strongly correlated Bloch states at low temperature. Below ~ 30 K the resistivity of CeCoIn$_5$ is nearly linear in temperature, a functional dependence commonly found in magnetically mediated superconductors and frequently associated with the proximity to a quantum critical point [28, 41]. The low value of ρ at ~ 2.4 K (~ 3 $\mu\Omega$cm) indicates minimal defect scattering. The inset of figure 6.2 reveals clear evidence for superconductivity: zero resistance is achieved at ~ 2.3 K.

6.2 Results for Magnetic Susceptibility

The details about the AC susceptibility measurements can be found in section 4.2.1 and in the reference [22]. A similar cooling/warming technique was used as for the resistivity measurement. Several chips of CeCoIn$_5$ were glued with 5-minute epoxy (Mastercraft) on a Saphire rod (see Figure 6.3) which was thermally anchored to the bolometer stage inside the ^{3}He cryostat. The system was then cooled down to 0.5 K (for cooling see section 3.2) and after stabilizing, the temperature was allowed to increase slowly.

Results for two different sets of crystals can be seen in Figures 6.4 and 6.5. In each Figure we observe a superconducting transition taking place at $T_c \sim 2.3$ K, which confirms the result from the resistivity experiments and is again in very good agreement with the known literature value. (These are "raw" data, uncorrected for the influence of empty coils or their geometry, used only to observe the change in the response of the

experimental system at the transition temperature.) The orientation of the magnetic field during the measurement was approximately perpendicular to the ab-plane of the crystals.

Note the two steps - two transitions - in Figure 6.5. The change in the magnetic susceptibility at ~ 3.4 K is due to an uncleaned remaining trace amount of pure Indium flux on the sample. This is due to the fact, that the crystals with the best surfaces were saved for the optical measurements. In spite of careful cleaning there was still some Indium remaining in microscopic holes on the rough surface of the small pieces used for the ac-susceptibility experiments. The ac-susceptibility thus reflects the transition to the superconducting state of Indium at 3.4 K.
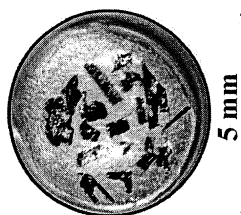
Figure 6.3: **Chips of CeCoIn$_5$ for measuring the magnetic susceptibility** χ

6.3 Conclusion from the Electric and Magnetic Experiments

Both of the experiments confirmed there is a superconducting transition in the examined sample of CeCoIn$_5$. The transition temperature was observed at T$_c$ = 2.3 K. This information confirms the quality of the samples used for the more complex experiments of the optical properties of CeCoIn$_5$ above and below the transition temperature. The results of the optical measurements in the FIR region are presented in the following sections.
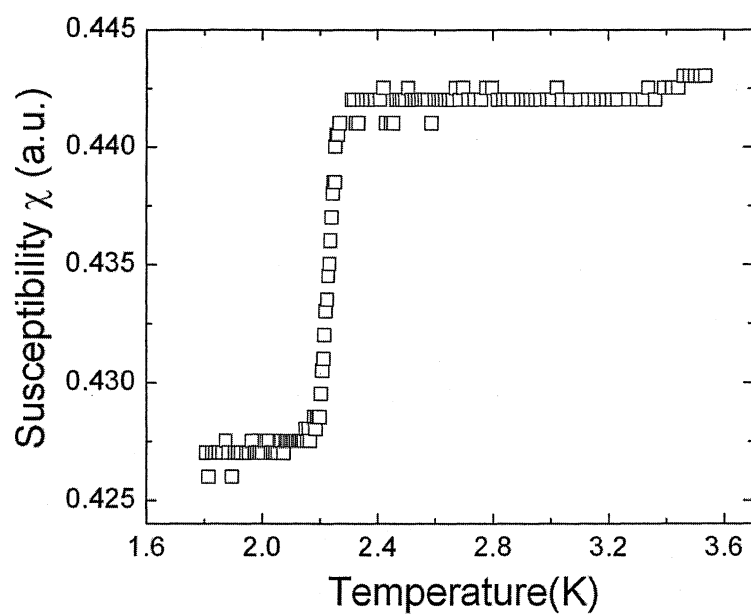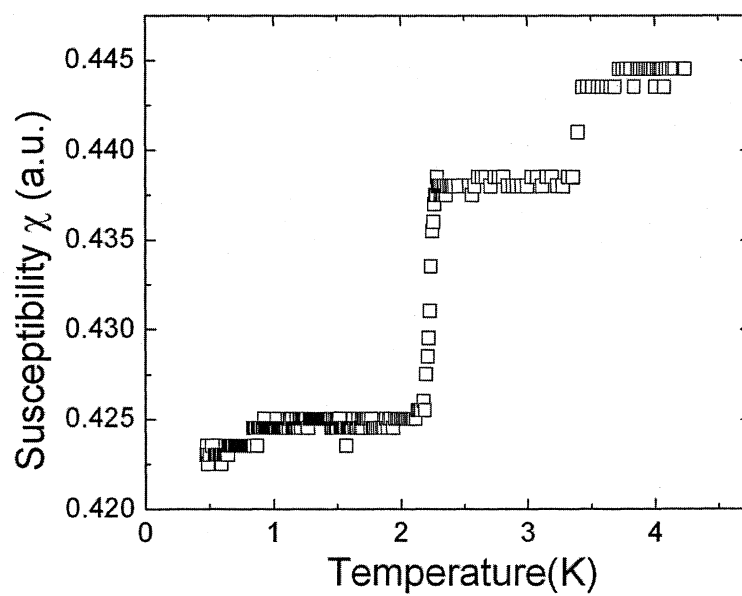
Figure 6.4: **The magnetic susceptibility for CeCoIn$_5$**

Figure 6.5: **The magnetic susceptibility for CeCoIn$_5$ with Indium**

6.4 The FIR Optical Measurements

6.4.1 The Sample for the Optical Experiments

To carry out optical measurements on any material one must have a flat sample of good quality and of proper dimensions. The samples of CeCoIn$_5$ are small thin platelets with usual dimensions of 1 mm $\times$ 1 mm, or 1 mm $\times$ 2 mm. To increase the total reflecting surface, a mosaic was built out of several pieces of CeCoIn$_5$. One such a mosaic with area $\sim$ 4 mm $\times$ 4 mm can be seen in Figure 6.6. The yellowish material is the 5 minute epoxy used to glue the sample to the copper post. All the optical experiments were performed on mosaics of CeCoIn$_5$.
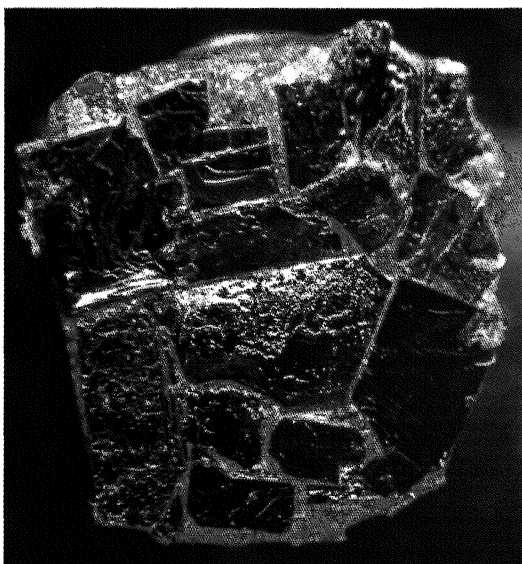
Figure 6.6: **Mosaic of CeCoIn$_5$ samples for optical measurements**

6.4.2 Thermal Reflectance

As has been already discussed in section 2.3 the first step involved in determining the reflectance of a given sample is to measure the ratio of the intensity of light reflected

from the sample to the intensity of light reflected from a reference mirror. This RATIO is given by the following formula

$$RATIO = \frac{Reflectance\ (sample)}{Reflectance\ (mirror)}. \tag{6.1}$$

An example of experimental data of such a ratio for $CeCoIn_5$ in the range of approximately (20 - 200) cm^{-1} at 0.5 K in the superconducting state and at 2.5 K in the normal state can be seen in Figure 6.7.
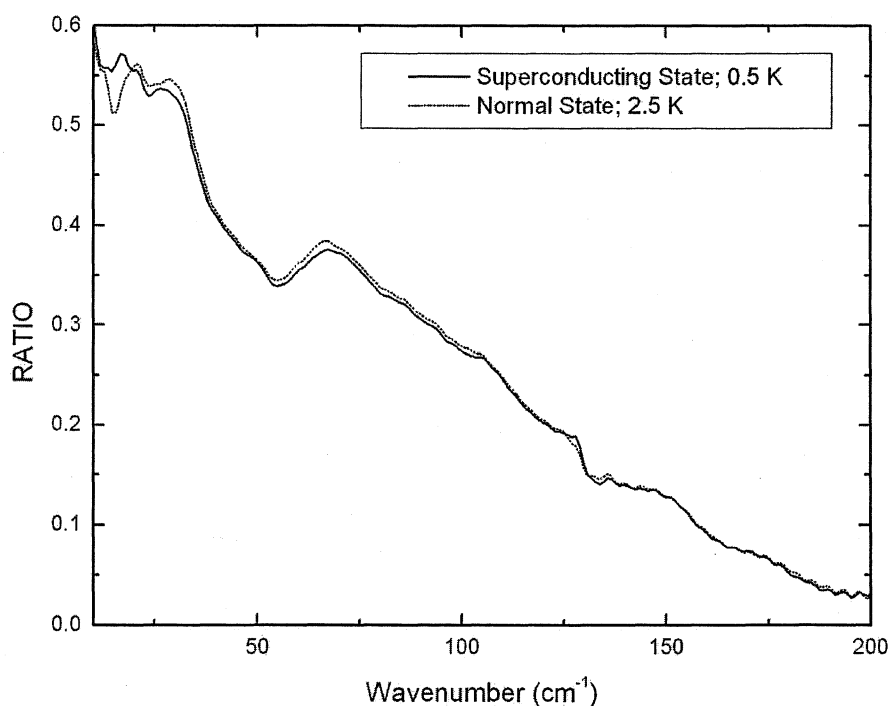

Figure 6.7: **The example of the RATIO-s for CeCoIn$_5$**

If we divide two RATIO-s given by equation 6.1 obtained at different temperatures, we will obtain the so-called "Thermal Reflectance". Thermal reflectance can be used to compare the properties of the material in two different states. In this thesis it is used to compare the superconducting state to the normal state of the given sample. An example of the thermal reflectance at low frequencies can be seen in Figure 6.8. The thermal
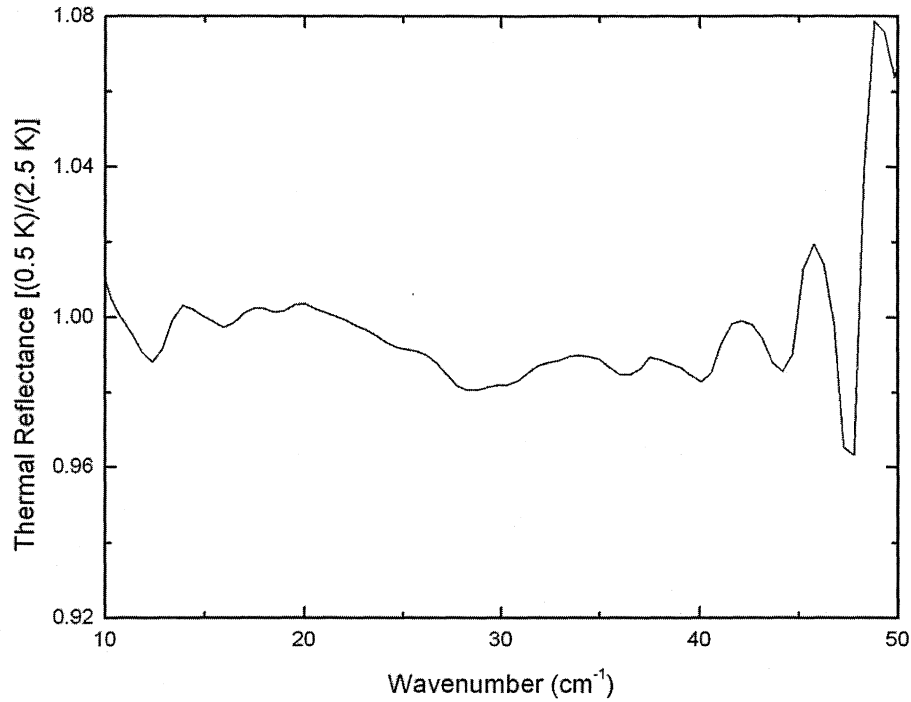
Figure 6.8: **The example of thermal reflectance for CeCoIn$_5$**

reflectance will reveal any change in the reflectivity below T$_c$. The optical functions are interdependent, which means a change in the reflectance is the equivalent of a change in the complex conductivity (or the complex refractive index), which of course reflects changes in the electron energy states in the material.

If there is no change in the optical properties at the two temperatures, the thermal reflectance would be unity for all wavenumbers. In practice there is always noise. If there is a temperature dependent change above the level of the noise in the spectra, this will be seen in the thermal reflectance as a distinct change in the region of relevant wavenumbers. The thermal reflectance presented in this thesis is always the ratio of the superconducting state (below T$_c$ at T = 0.5 K) with respect to the normal state (above T$_c$ at T = 2.5 K).

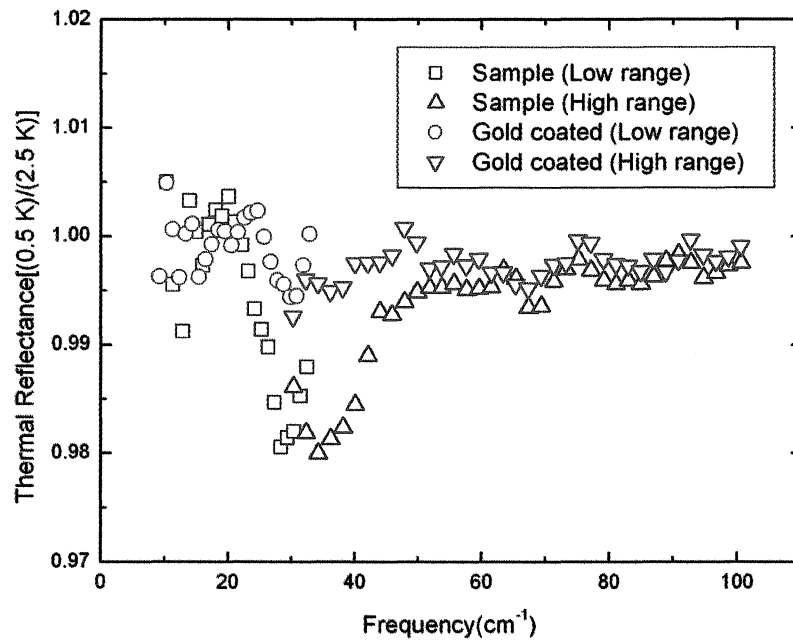The final result can be seen in Figure 6.9. This is the composite thermal reflectance

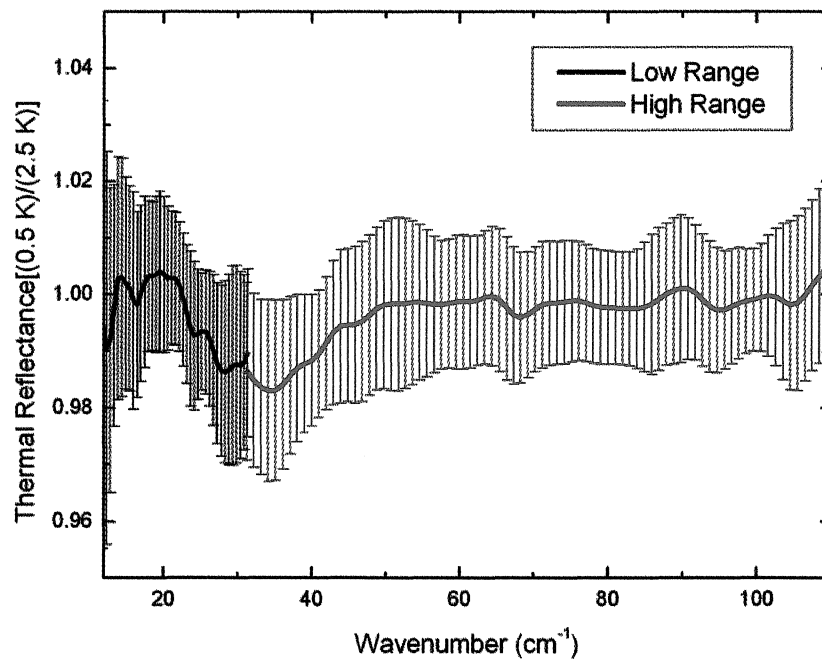Figure 6.9: **The resultant thermal reflectance of CeCoIn$_5$ and of the gold coated sample**

Figure 6.10: **Thermal reflectance of CeCoIn$_5$ with the uncertainties**

obtained for one completed set of experiments carried out in two regions of the FIR. The first region being approximately (10 - 30) cm^{-1} and the second region being approximately (30 - 100) cm^{-1}. For the filtering the fluorogold with black polypropylene (cut-off frequency $\sim$ 60 cm^{-1}) and the diamond powder with the black polypropylene (cut-off frequency $\sim$ 250 cm^{-1}) filters were used, respectively. The discrepancy between cut-off frequencies and the frequency ranges of the resultant thermal reflectance is due to the increasing noise, as one approaches the cut-off frequency of a given filter. (It should be mentioned here, that due to the mosaic nature of the sample and the resulting very small signals, to get this result 83 ratios of the low frequency range and 50 ratios of the high frequency range were recorded within a time period of 2 weeks. One ratio here represents two step-and-integrate scans of the reflectance of the sample and one scan of the reflectance of the mirror.) As we can see there is an apparent change in the thermal reflectance below 50 cm^{-1}.

The thermal reflectance of CeCoIn$_5$ is shown together with the thermal reflectance of the gold coated sample, which allows one to make a simple comparison with a very good reflector in the FIR. The same experiments were carried out on the gold coated sample as on the uncoated sample for a similar period of time. As can be seen from Figure 6.9 the feature is not present for the gold coated sample and the thermal reflectivity is close to a unity, a behavior expected for an ideal mirror-like surface, with no temperature dependence.

In Figure 6.10 we can see the uncertainties calculated for both ranges (low and high) before the data were processed to make a smooth function with no discontinuities that could be used for the Kramers-Krönig analysis. Standard deviations for both of the ranges are below the value of 1.5 %. The data plotted together with the error bars still preserve the decrease in the reflectance below $\sim$ 50 cm^{-1}.

6.4.3 Absolute Reflectance

To obtain the absolute reflectance of the sample the gold evaporation technique described in section 2.3 can be used. However, the small dimensions of the mosaic sample used in the optical measurements and the small change in superconducting state reflectance with respect to the normal state, made it difficult to extract the absolute reflectance, because the small difference is lost in the noise. That is, further division of the sample RATIO by the one for the gold-coated sample according to the procedure outlined in section 2.3 to obtain the absolute reflectance resulted in severe amplification of the noise, which made the use of this procedure impossible.

Another possibility is to make use of the reflectance data for the sample in the normal state, if this is available in the literature. In this case, the thermal reflectance data are multiplied with the absolute normal state reflectance of the sample itself. This yields the absolute reflectance in the superconducting state. Singley *et al* [38] carried out optical measurements on CeCoIn$_5$ in a wide range of frequencies and temperatures. To extract the superconducting state absolute reflectance we used their lowest temperature (10 K) and lowest frequency data (25 - 100 cm^{-1}). The procedure is outlined in section 6.4.4. Once the absolute superconducting state reflectance is known, Kramers-Krönig analysis can be used to obtain the optical conductivity. However, in order to perform the Kramers-Krönig analysis one must have as wide a range of data as possible. (Outside the range of available experimental data extrapolations must take place.) We used the reflectance of Singley *et al* at T = 10 K in the range (25, 2000) cm^{-1} (see Figure 6.11) and their room temperature reflectance from 2000 cm^{-1} to 48800 cm^{-1} (see Figure 6.12). At high enough frequencies the reflectance usually loses its temperature dependence justifying the use of the high temperature data as the direct extrapolation for the low temperature data. In the low frequency region, where there is a strong temperature dependence, one must be much more careful. Here we have assumed that since the temperature difference
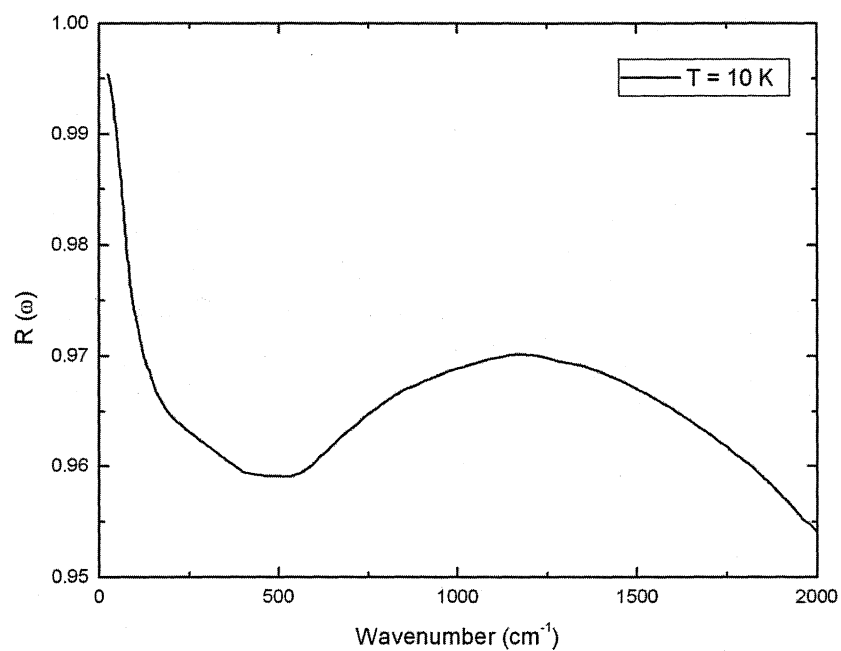
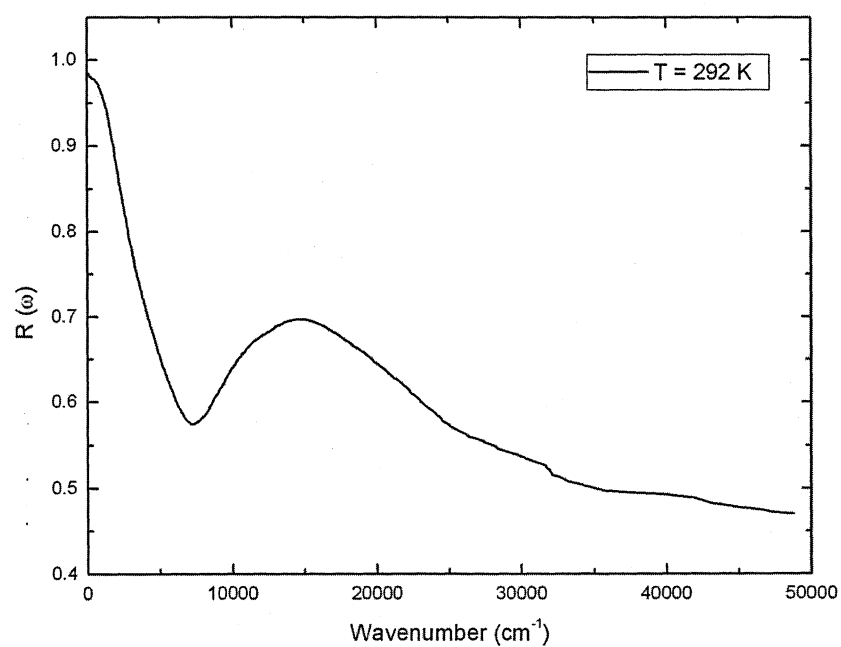Figure 6.11: **Reflectance of the CeCoIn$_5$ in the range (25, 2000)cm^{-1} [38]**

Figure 6.12: **Reflectance of the CeCoIn$_5$ in the range (100, 48800)cm^{-1} [38]**

between our normal state (2.5 K) and that of Singley *et al* (10 K) is not too big, that we are justified in using Singley *et al*'s low frequency data to extract our superconducting state data. Furthermore, we assume, that Singley *et al*'s 10 K normal state data from 100 cm^{-1} to 2000 cm^{-1} is a valid extension for our extrapolated superconducting state data.

Taking Singley *et al*'s two sets of data as a starting point, some manipulation was required before KK analysis could be carried out. To be successful with the KK analysis the extrapolations in the low frequency range (down to zero) and in the high frequency range (until the reflectance decreases enough that free-electron behavior can be assumed) must still be performed. Furthermore all regions of the reflectance, the modeled and the measured ones must be linked, to make a smooth function without discontinuities.

To ensure that our extrapolations are reasonable we first attempted to reproduce the optical conductivity obtained by Singley *et al*. In the low range of frequencies a Hagen-Rubens reflectance with $\rho = 6\mu\Omega cm$ was used to extrapolate the data down to zero frequency. In the high frequency range, the tail of Singley *et al*'s data ([38]) was fit with a decreasing power law ($\omega^{-0.30062}$). To overcome the difference in absolute reflectance between the low temperature and high temperature data sets of Singley *et al* at 2000 cm^{-1}, the high temperature data was modeled in two different ways (see below) to decrease more quickly towards the low frequencies (between 2000 cm^{-1} and 15000 cm^{-1}). The software used for the Kramers-Krönig calculations requires the different regions of the reflectance to contain not more than 1024 points. The reflectance was therefore divided into several files of different frequency increments. One of the resulting absolute reflectances consisting of these files can be seen in Figure 6.13. This normal state absolute reflectance was then used for Kramers-Krönig analysis to calculate the optical functions.

As has been already mentioned above, the data set of Singley *et al* for the high
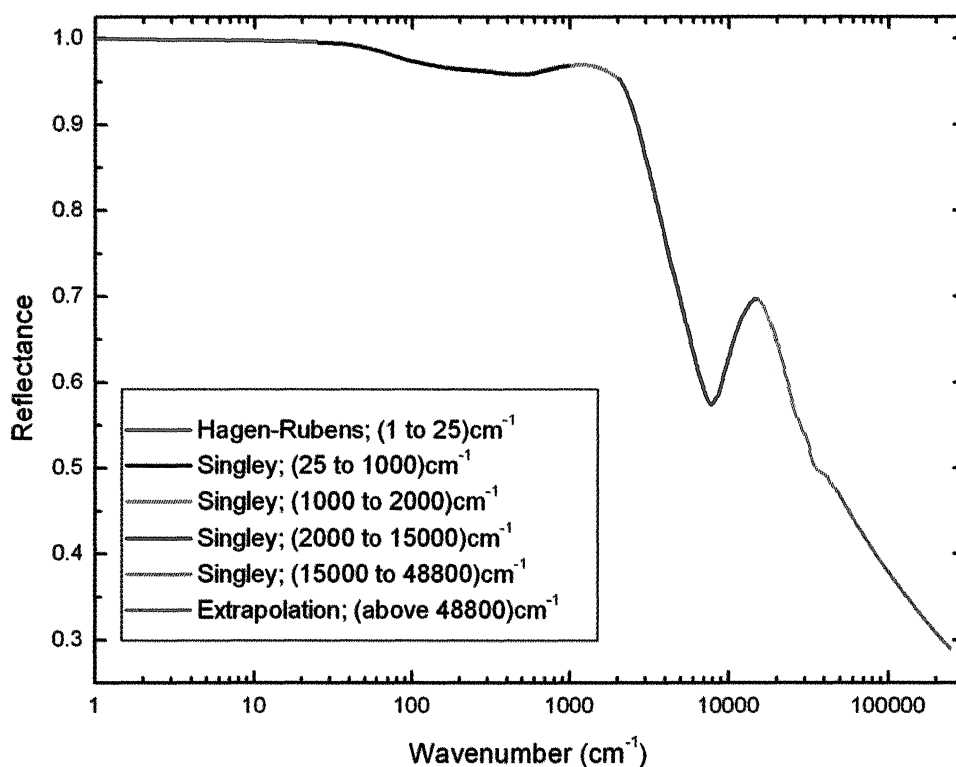
Figure 6.13: **Absolute reflectance of CeCoIn$_5$; Experimental data and extrapolations**

frequency range (2000 cm^{-1} - 48800 cm^{-1}) was modeled in two different ways to link with the low frequency data (25 - 2000)cm^{-1}. In the first model a constant value of 900 cm^{-1} was added to all of the wavenumbers thus creating a shift of the whole function towards high frequencies. In the second model the high frequency data set was divided into two regions, the first one in the range (2000 - 15000)cm^{-1} and the second one (15000 - 48800)cm^{-1}. Only the values for reflectance in the region (2000 - 15000)cm^{-1} have been changed, thus leaving the rest of the high frequency range of Singley *et al*'s data unchanged. This approach assures, that the significant peak at $\sim$ 17000 cm^{-1} is not affected by the change in the function. The values for (2000 - 15000)cm^{-1} were changed with a function $f = \nu + 900\times[1 - (\nu - 1100\text{cm}^{-1})/13900 \text{ cm}^{-1}]$, resulting in a smooth connection to the previous data set (25 - 2000)cm^{-1}. Both of the models were used for

KK analysis with several different extrapolations in the low and high frequency limit.

This process was repeated several times to get the best match with Singley *et al*'s data. The best two results for the calculated real part σ_1 of the complex conductivity are shown compared with the real part of the optical conductivity obtained by Singley *et al* in Figures 6.14 and 6.15. As can be seen, the results match quite well. Since the extrapolation used in Figure 6.14 matches better at low frequencies, we chose that for the Kramers-Krönig analysis of the superconducting state, which is presented in the following section.

6.4.4 Kramers-Krönig Analysis for the CeCoIn$_5$

The data shown in Figure 6.9 were used to calculate the optical functions in the superconducting state. First the thermal reflectance was smoothed to suppress noise (see Figure 6.16). Then it was multiplied with the extrapolated low frequency data of Singley *et al* [38] to gain the absolute reflectance of the sample in the superconducting state. The result can be seen in Figure 6.17. Note that data below 25 cm^{-1} is not reliable since it is derived from extrapolations to Singley *et al*'s data. The absolute reflectance was then extrapolated at lower and higher frequencies as discussed in the preceding section. The resultant data were used for Kramers-Krönig analysis. The real part of the optical conductivity obtained is shown in figure 6.18. The low frequency data is shown in Figure 6.19. (The data for wavenumbers less than 25 cm^{-1} were omitted, because they are not believed to be reliable due to a lack of normal state data in this region.) As we can see, there is a significant difference between the real part of the conductivity in the normal and superconducting state in the low frequency range (25 - 75)cm^{-1} with a peak in the conductivity at ~ 50 cm^{-1}. This behavior may be due to the opening of an energy gap in the spectrum of excitations, however repetition of the optical measurement must be performed to confirm this result.
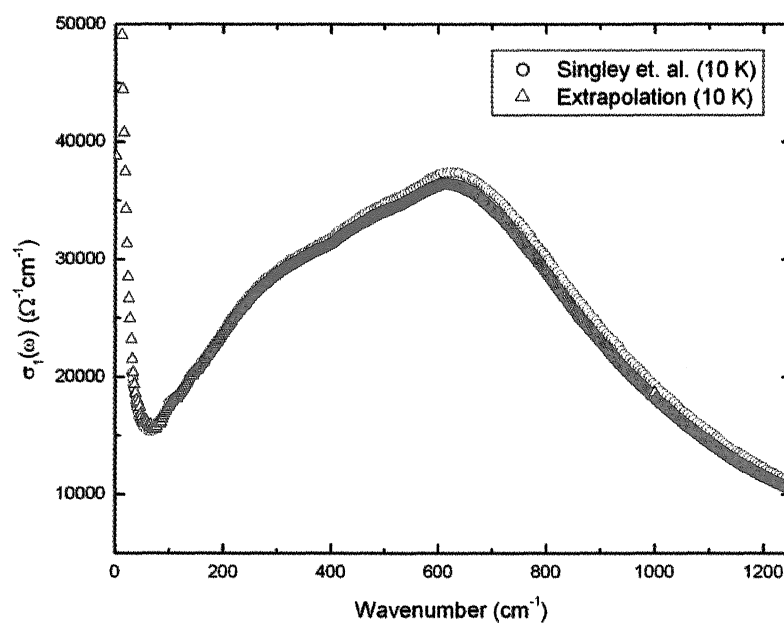
Figure 6.14: **Calculated real part of the complex conductivity according to [38]; first fit**
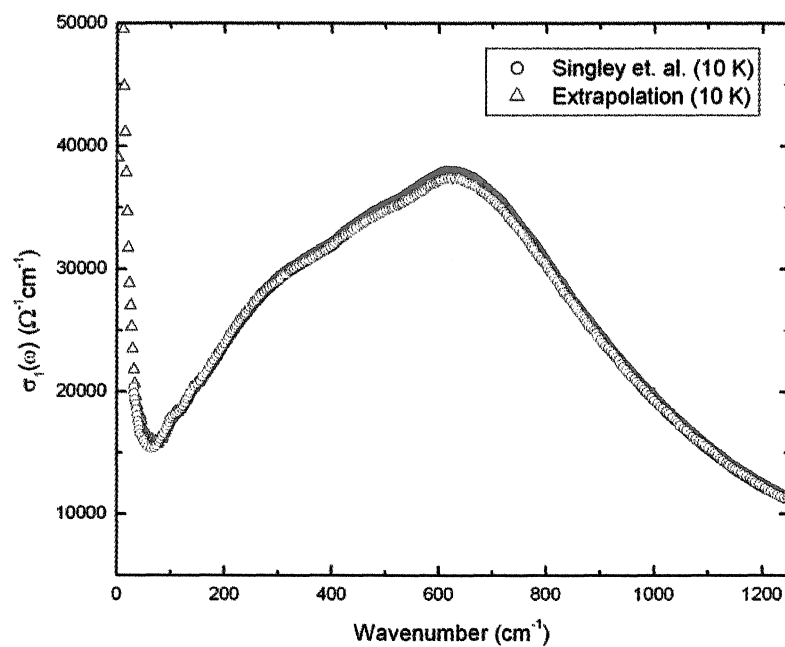

Figure 6.15: **Calculated real part of the complex conductivity according to [38]; second fit**
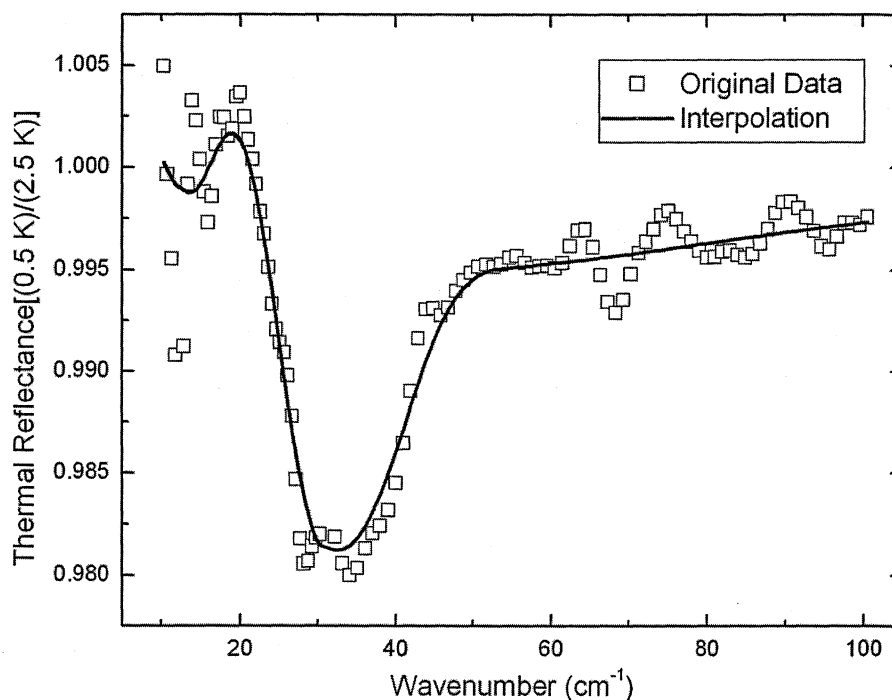
Figure 6.16: **Smoothed thermal reflectance of CeCoIn$_5$**

It is very important to note here, that this effort to obtain the superconducting state optical conductivity from our data can not be understood as an exact result, but rather represents a best estimate with several caveats as discussed above. That said, this still represents a very significant result, because to our knowledge, no other experimental system is capable of carrying out absolute reflectance measurement at these low temperatures and frequencies. Suggestions for further work include measuring a larger mosaic and/or large single crystals to confirm the thermal reflectance result of Figure 6.9 and if possible to obtain the absolute reflectance directly, both above and below T$_c$. Measurements of intermediate temperatures would also be valuable to see the temperature evolution of this feature.
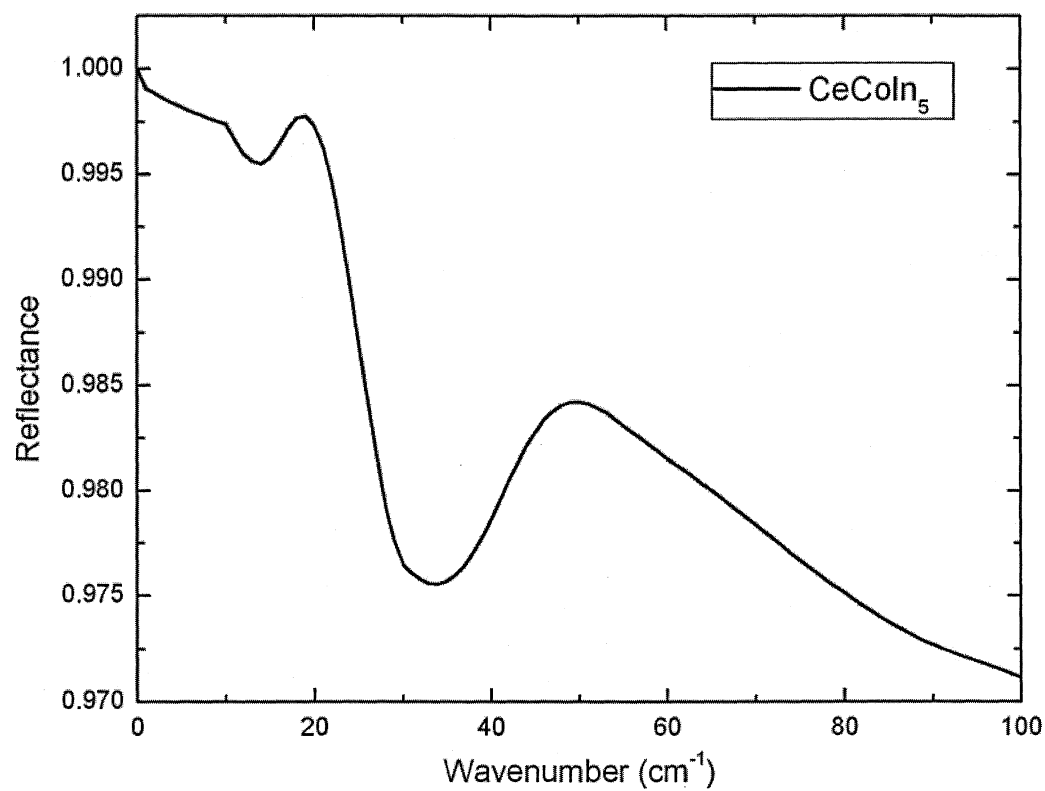
Figure 6.17: **Experimental absolute reflectance for CeCoIn$_5$ with the low frequency extrapolation**
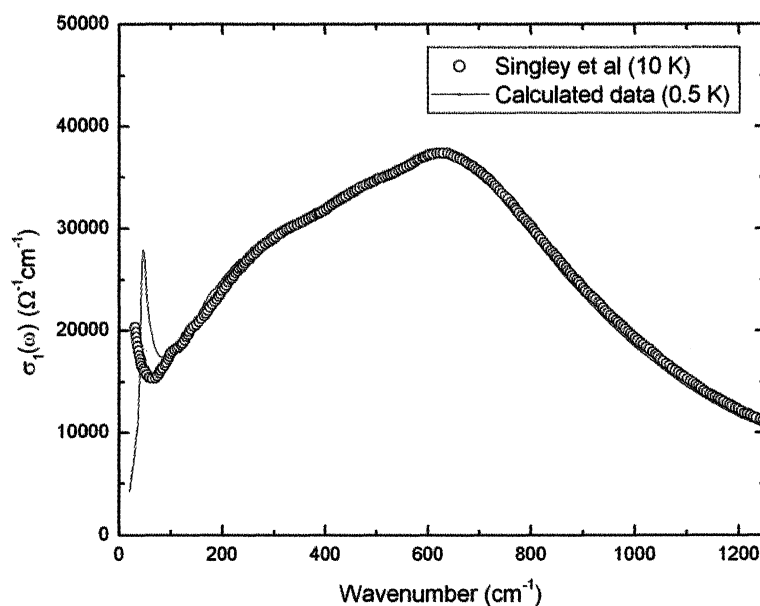
Figure 6.18: **Calculated real part of the complex conductivity from experimental data**
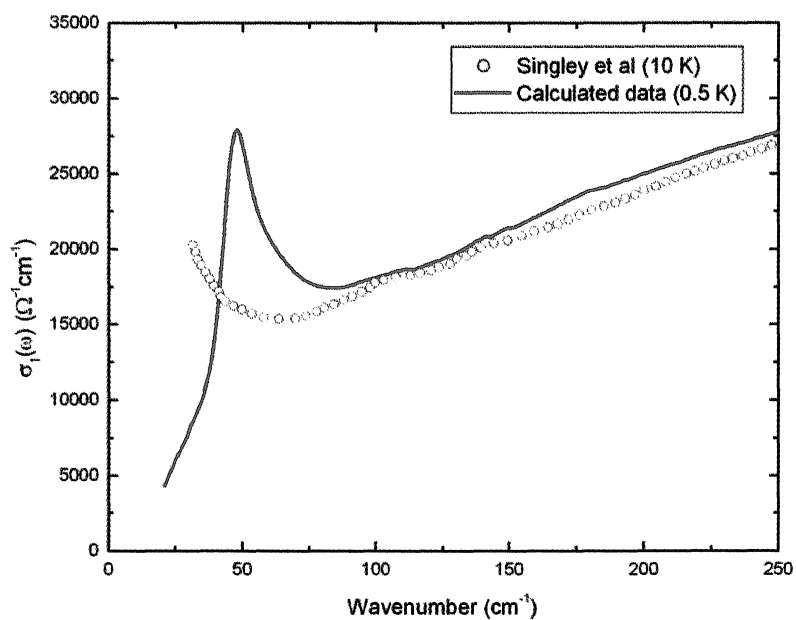

Figure 6.19: **Calculated real part of the complex conductivity from experimental data; Low frequency region**

Chapter 7

Concluding Remarks

The optical experiments on heavy-fermion superconductor $CeCoIn_5$ in the FIR indicate the opening of some type of an energy gap close to $\nu \sim 50$ cm^{-1}. The thermal reflectance obtained in the range of (10, 100)cm^{-1} clearly reveals a change in the superconducting state reflectance compared to the normal state reflectance of $CeCoIn_5$ below 50 cm^{-1}. Although the assumptions made in order to perform the Kramers-Krönig analysis imply some uncertainty, these calculations can give us a reasonable first estimate of the optical conductivity in the superconducting state. We note two important facts at this point:

1) The extrapolations for the low frequency range (towards zero frequency) and for the high frequency range (decrease in reflectance in accordance with free-electron behavior) are common to all Kramers-Krönig (KK) analysis. One must perform these extrapolations in order to gain the infinite range of frequencies required to compute the corresponding KK integrals. These extrapolations imply that any time Kramers-Krönig analysis is used it gives only an estimate for the final function and not an exact value (though it may be very close to the exact value).

2) The data used for the interval, that is of greatest interest, are obtained from our measurements. This means, that even though the resultant real conductivity function is not exact (due to the extrapolations used), the experimental change occurring in the reflectance of $CeCoIn_5$ upon entering the superconducting state will manifest itself in the optical conductivity as well.

Further evidence for the feature observed in the thermal reflectance of $CeCoIn_5$ can

be found through comparison with an earlier experiment. Unfortunately, (due to a weak signal, bad S/N ratio, and technical problems during the experiment) the resultant thermal reflectance contains strong fringes. Still, after performing KK analysis on this earlier data set (the same procedure was used), there is an evidence for a suppression in the real part of the complex conductivity $\sigma(\omega)$ at low frequencies.

Although the presence of the gap has not been incontrovertibly established, some comparisons with other work can be made, which suggest that the results of the very far IR spectroscopy measurements of CeCoIn$_5$ are of considerable interest.

The frequency regime where we find a difference in the superconducting state reflectance and the normal state reflectance was also found to be of interest in the normal state data of Singley *et al.* They identified the minimum in the optical conductivity near 60 cm^{-1} (as can be seen in Figure 6.19) to a Holstein band. They suggested this Holstein band could arise from the coupling of antiferromagnetic spin fluctuations to the heavy quasi-particles.

Rourke *et al* carried out point-contact spectroscopy measurements on CeCoIn$_5$ [50]. They observed an energy gap around 3 meV, which they attributed to the superconducting energy gap. Since tunneling experiments measure Δ, this would correspond to an energy of 6 meV ($\sim$ 48 cm $^{-1}$) in optical spectroscopy [51], which measures 2Δ. This is in very good agreement with the feature in our work.

The question that remains open is the character of this energy gap (assuming further work supports its existence). That is, whether it is attributable to the superconducting energy gap, as might be suggested by comparison with the tunneling work, or to the opening of a gap in the spectrum of magnetic excitations.

Bonn *et al* [52] observed similar behavior for heavy-fermion metal URu$_2$Si$_2$ (exhibiting both superconducting and magnetic ordering). They observed in the real conductivity the development of a peak close to 60 cm^{-1}, followed by a strong suppression below this

frequency, as the temperature was lowered below the Néel temperature (T_N = 17.5 K). The shape of their conductivity is very similar to our own data. Taking into account the work of Sidorov *et al* [53], there is a belief that CeCoIn$_5$ is in a state close to an antiferromagnetic (AFM) QCP (*i.e.* the development of an AFM state for T → 0 K) at atmospheric pressure. According to their assumptions, the AFM transition for heavy-fermion CeCoIn$_5$ may be at an inaccessible slightly negative pressure. (This conclusion is made upon the comparison of CeCoIn$_5$ to CeRhIn$_5$. CeCoIn$_5$ has a 1.7% smaller cell volume than isostructural CeRhIn$_5$. CeRhIn$_5$ is antiferromagnetic, but it becomes a pressure-induced unconventional superconductor at ∼ 1.6 GPa. For more details see [53].) They present a phase diagram which shows the opening of a pseudogap just above the superconducting transition temperature T_c, a situation that is similar to the cuprates. Confirmation of the existence of an energy gap close to 50 cm^{-1} in CeCoIn$_5$, would provide a new challenge for the theory in the field of heavy fermion physics.

To further investigate this interesting feature, improvements in the experiment must be accomplished. One is to build up a bigger mosaic, and - if possible - out of bigger single crystals (or, ideally to carry out measurements on a single large crystal). This would improve the S/N ratio and enable one to determine the absolute reflectance of the sample directly from the measurements. Further suggestions are to carry out experiments in a wider range of frequencies and to run measurements at several temperatures below T_c to observe the temperature evolution of this feature.

Appendix A

Fourier Analysis

A.1 Fourier Series

Fourier series are expansions of periodic functions f(x) in terms of an infinite sum of sines and cosines of the form [46]

$$f(x) = \sum_{n=0}^{\infty} a'_n \cos(nx) + \sum_{n=0}^{\infty} b'_n \sin(nx) \tag{A.1}$$

Fourier series make use of the orthogonality relationships of the sine and cosine functions, which can be used to calculate the coefficients a'_n and b'_n in the sum. The computation and study of Fourier series is known as harmonic analysis.

To compute a Fourier series, use the integral identities:

$$\int_{-\pi}^{\pi} \sin(mx)\sin(nx)dx = \pi\delta_{mn} \qquad n, m \neq 0 \tag{A.2}$$

$$\int_{-\pi}^{\pi} \cos(mx)\cos(nx)dx = \pi\delta_{mn} \qquad n, m \neq 0 \tag{A.3}$$

$$\int_{-\pi}^{\pi} \cos(mx)\sin(nx)dx = 0 \tag{A.4}$$

$$\int_{-\pi}^{\pi} \sin(mx)dx = 0 \tag{A.5}$$

$$\int_{-\pi}^{\pi} \cos(mx)dx = 0 \tag{A.6}$$

where δ_{mn} is the Kronecker delta. Now, expand the function f(x) as an infinite series of the form:

$$f(x) = \sum_{n=0}^{\infty} a'_n \cos(nx) + \sum_{n=0}^{\infty} b'_n \sin(nx) = \frac{1}{2}a_0 + \sum_{n=1}^{\infty} a_n \cos(nx) + \sum_{n=1}^{\infty} b_n \sin(nx) \tag{A.7}$$

where we have related the $a_0 = 2a_0'$ term for future convenience but set $b_n = b_n'$ and left $a_n = a_n'$ for n $\geq$ 1. Using the identities in (A.2 - A.6) we can write:

$$a_0 = \frac{1}{\pi} \int_{-\pi}^{\pi} f(x) dx \tag{A.8}$$

$$a_n = \frac{1}{\pi} \int_{-\pi}^{\pi} f(x) \cos(nx) dx \tag{A.9}$$

$$b_n = \frac{1}{\pi} \int_{-\pi}^{\pi} f(x) \sin(nx) dx \tag{A.10}$$

for n = 1, 2, 3, ... The series expansion converges to the function $\overline{f}$ (equal to the original function at points of continuity or to the average of the two limits at points of discontinuity) if the function satisfies the Dirichlet conditions [46].

For a function f(x) periodic on an interval $[-L, L]$, use a change of variables to transform the interval of integration from $[-\pi, \pi]$ to $[-L, L]$. Let

$$x \equiv \frac{\pi x'}{L} \tag{A.11}$$

$$dx \equiv \frac{\pi dx'}{L} \tag{A.12}$$

Solving for x', $x' = \frac{Lx}{\pi}$. Plugging this in gives:

$$f(x') = \frac{1}{2}a_0 + \sum_{n=1}^{\infty} a_n \cos(\frac{n\pi x'}{L}) + \sum_{n=1}^{\infty} b_n \sin(\frac{n\pi x'}{L}) \tag{A.13}$$

The notation of a Fourier series can also be extended to complex coefficients. Consider a real-valued function f(x)

$$f(x) = \sum_{n=-\infty}^{\infty} A_n e^{inx} \tag{A.14}$$

where

$$A_n = \frac{1}{2\pi} \int_{-\pi}^{\pi} f(x) e^{-inx} dx \tag{A.15}$$

For a function periodic in $[-\frac{L}{2}, \frac{L}{2}]$ these become:

$$f(x) = \sum_{n=-\infty}^{\infty} A_n e^{i2\pi nx/L} \tag{A.16}$$

$$A_n = \frac{1}{L} \int_{-\frac{L}{2}}^{\frac{L}{2}} f(x)e^{-i2\pi nx/L}dx \tag{A.17}$$

These equations are the basis set for the extremely important Fourier transform, which is obtained by transforming A_n from discrete variable to a continuous one as the length L $\rightarrow \infty$.

A.2 Fourier Transform

The Fourier transform is a generalization of the complex Fourier series in the limit as the length of the interval L $\rightarrow +\infty$. Replace the discrete A_n with the continuous F(k)dk while letting $\frac{n}{L} \rightarrow$ k. Then change the sum to an integral, and the equations become [46]

$$f(x) = \int_{-\infty}^{\infty} F(k)e^{i2\pi kx}dk \tag{A.18}$$

$$F(k) = \int_{-\infty}^{\infty} f(x)e^{-i2\pi kx}dk \tag{A.19}$$

Here,

$$F(k) = \mathcal{F}_x[f(x)](k) = \int_{-\infty}^{\infty} f(x)e^{-i2\pi kx}dx \tag{A.20}$$

is called the forward (-i) Fourier transform, and

$$f(x) = \mathcal{F}_k^{-1}[F(k)](x) = \int_{-\infty}^{\infty} F(k)e^{i2\pi kx}dk \tag{A.21}$$

is called the inverse (+i) Fourier transform. Note that some authors (especially physicists) prefer to write the transform in terms of angular frequency $\omega = 2\pi\nu$ instead of the oscillation frequency ν. However, this destroys the symmetry, resulting in the transform pair

$$H(\omega) = \mathcal{F}[h(t)] = \int_{-\infty}^{\infty} h(t)e^{-i\omega t}dt \tag{A.22}$$

$$h(t) = \mathcal{F}^{-1}[H(\omega)] = \frac{1}{2\pi} \int_{-\infty}^{\infty} H(\omega)e^{i\omega t}d\omega \tag{A.23}$$

To restore the symmetry of the transforms, the convention

$$g(y) = \mathcal{F}[f(t)] = \frac{1}{\sqrt{2\pi}} \int_{-\infty}^{\infty} f(t)e^{-iyt}dt \tag{A.24}$$

$$f(t) = \mathcal{F}^{-1}[g(y)] = \frac{1}{\sqrt{2\pi}} \int_{-\infty}^{\infty} g(y)e^{iyt}dy \qquad (A.25)$$

is sometimes used [46].

A function f(x) has a forward and inverse Fourier transform such that:

$$f(x) = \begin{cases} \int_{-\infty}^{\infty} e^{2i\pi kx}[\int_{-\infty}^{\infty} f(x)e^{-2i\pi kx}dx]dk & \text{for f(x) continuous at x} \\ \frac{1}{2}[f(x_+) + f(x_-)] & \text{for f(x) discontinuous at x} \end{cases} \qquad (A.26)$$

provided that:

1) integral exists

2) There is a finite number of discontinuities.

3) The function has bounded variation. A sufficient weaker condition is fullfilment of the Lipschitz condition [46].

A.3 Fourier Transform - Simple Example

In the precedent sections we could see how FT is defined and how it works from mathematical pont of view. For better understanding, let us consider one quite simple composite signal. Suppose we have three sinusoidal signals:

$$f_1(x) = \sin(1Hz) \qquad (A.27)$$

$$f_2(x) = \frac{1}{3}\sin(3Hz) \qquad (A.28)$$

$$f_3(x) = \frac{1}{5}\sin(5Hz) \qquad (A.29)$$

which can be seen in Figure A.1 (a). If we mix these signals together, we will have a single composite signal, which can be seen in Figure A.1 (b). We can express this signal as

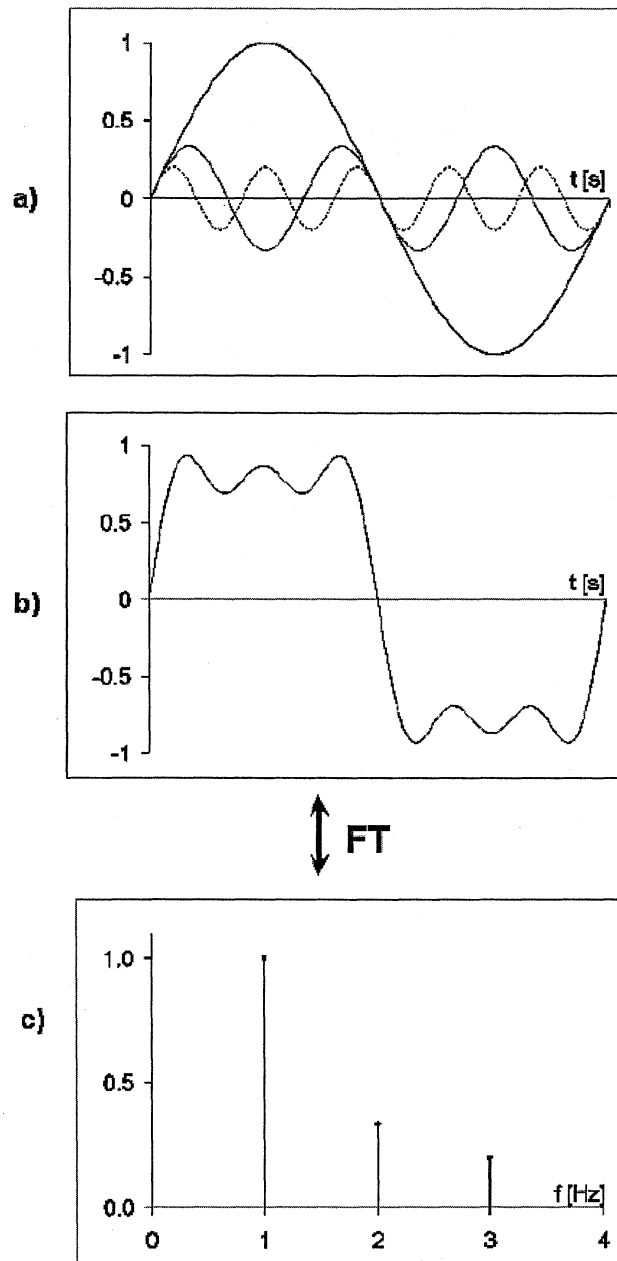$$F(x) = f_1(x) + f_2(x) + f_3(x) = \sin(1Hz) + \frac{1}{3}\sin(3Hz) + \frac{1}{5}\sin(5Hz) \qquad (A.30)$$

Figure A.1: The simple example for the process of Fourier Transform.

a) Three sinusoidal signals

b) Their time representation

c) Their frequency representation

This can be understood as the time (or space) domain representation of measured signal. Straight from its mathematical expression, we can think about this signal in other domain - we can think about it as a sum of different frequencies with various amplitudes. Thus, there are two (equivalent) ways of thinking (Figure A.1 (b) and (c)). We can work with the signal (record it) as time dependant deviation, or as a sum of frequencies. The technique for changing the signal from one domain to another one is the Fourier Transform.

Note the shape of the signal in Figure A.1, it looks similar to the so-called boxcar function

$$B(x) = \sum_{n=0}^{\infty} \frac{\sin[(2n+1)Hz]}{2n+1} \qquad (A.31)$$

actually, the trial signal is a a part of this sum. This simmilarity is not a coincidence and the example has been chosen on purpose. Boxcar function is a typical example used in any introduction to FTS (*i.e.* see Willimas [4]). It's easy to build up this function according to formula A.31, but it is bringing another difficulty with it - so called Gibbs phenomenon (see section 1.3.8 or Griffiths [8] for more details).

Appendix B

Cauchy's Integral Formula

Let f be analytic in the simply connected domain D, and let C be a simple closed positively oriented contour that lies in D. If z_0 is a point that lies interior to C, then [47]

$$f(z_0) = \frac{1}{2\pi i} \int_C \frac{f(z)}{z - z_0} dz \qquad (B.1)$$

Appendix C

Interaction of Light with the Medium

We begin with the basic set of equations for electro-magnetism - the Maxwell's equations. We will consider, that there are no external sources ($\rho^{ext} = 0$) and that there is no spatial variation in ϵ (isotropic media) [48, 14, 12]. With these conditions, we can write the Maxwell's equations as

$$\nabla \cdot \mathbf{E} = 0 \tag{C.1}$$

$$\nabla \times \mathbf{E} = -\mu \frac{\partial \mathbf{H}}{\partial t} \tag{C.2}$$

$$\nabla \cdot \mathbf{H} = 0 \tag{C.3}$$

$$\nabla \times \mathbf{H} = \sigma \mathbf{E} + \epsilon \frac{\partial \mathbf{E}}{\partial t} \tag{C.4}$$

Using the vector identity

$$\nabla \times (\nabla \times \mathbf{E}) = \nabla(\nabla \cdot \mathbf{E}) - \nabla^2 \mathbf{E} \tag{C.5}$$

the equations predicting elecromagnetic waves may be obtained. These are

$$\nabla^2 \mathbf{E} - \epsilon\mu \frac{\partial^2 \mathbf{E}}{\partial t^2} - \mu\sigma \frac{\partial \mathbf{E}}{\partial t} = 0, \tag{C.6}$$

and a similar one for $\mathbf{H}$. The solution of equation C.6, which is most useful for us, describes a plane electromagnetic wave of angular frequency ω. For these waves $\mathbf{E}$ and $\mathbf{H}$ are perpendicular to each other and also to the direction of propagation. The solution

of C.6 at a point at distance z from a fixed origin measured along the direction of propagation has transverse components [14]

$$E = E_0 e^{i(qz - \omega t)} \tag{C.7}$$

where q is the wave vector and is defined as

$$q = \frac{2\pi}{\lambda} = \frac{\omega}{u} \tag{C.8}$$

u being the phase velocity and λ the wavelength. It is more general to write q as $\vec{q}$, the wave vector, which is given by

$$\vec{q} = \frac{\omega}{u^2} \vec{u} \tag{C.9}$$

Equation C.7 may be now written as

$$\mathbf{E} = \mathbf{E}_0 e^{i(\vec{q} \cdot \vec{r} - \omega t)} \tag{C.10}$$

A similar solution exists for the magnetic field $\mathbf{H}$ such that

$$\mathbf{H} = \frac{1}{\omega \mu} \mathbf{q} \times \mathbf{E} \tag{C.11}$$

The wave vector, or propagation constant, $\vec{q}$, can be expressed in terms of the electric and magnetic constants of the medium by differentiating eqn. C.7 and substituting in eqn. C.6, to give

$$q^2 = \omega^2 \mu (\epsilon + \frac{i\sigma}{\omega}) \tag{C.12}$$

To relate these quantities to the measurements which may be made in optical experiments, we remember, that for a non-absorbing medium, the refractive index is defined as c/u, where c is the speed of light in free space. For the absorbing case we define a complex refractive index $N = n + ik$, such that

$$N = n + ik = \frac{c}{u} = c \frac{|\mathbf{q}|}{\omega} \tag{C.13}$$

or

$$N^2 = \frac{c^2}{\omega^2}|\mathbf{q}|^2 \qquad (C.14)$$

where $c^2 = (\epsilon_0 \mu_0)^{-1}$. Using eqn. C.12 we obtain

$$N^2 = c^2 \mu (\epsilon + i\frac{\sigma}{\omega}) \qquad (C.15)$$

From equation C.15, the general relationship involving the index of refraction, dielectric function and complex conductivity can be determined. Let's rewrite this equation in a slightly different form

$$N^2 = (c^2 \mu_0 \epsilon_0) \mu_{rel} (\epsilon_{rel} + i\frac{\sigma}{\omega \epsilon_0}) = \mu_{rel} (\epsilon_{rel} + i\frac{\sigma}{\omega \epsilon_0}) \qquad (C.16)$$

Now we can define

$$(\epsilon_{rel} + i\frac{\sigma}{\omega \epsilon_0}) = \epsilon(\omega) \qquad (C.17)$$

where $\epsilon(\omega)$ is a complex dielectric function. Now we can write

$$N^2 = \mu_{rel}\epsilon(\omega) \qquad (C.18)$$

or as is usual in spectroscopy (after taking $\mu_{rel} = 1$, which is true in most of the cases)

$$N^2 = \epsilon(\omega) \qquad (C.19)$$

$$N(\omega) = \sqrt{\epsilon(\omega)} \qquad (C.20)$$

which will give us the following relations for complex refraction index $N(= n + ik)$ and complex dielectric function $\epsilon(= \epsilon_1 + i\epsilon_2)$

$$\epsilon_1 = n^2 - k^2 \qquad (C.21)$$

$$\epsilon_2 = 2nk \qquad (C.22)$$

$$n = \frac{1}{\sqrt{2}}[(\epsilon_1 + \epsilon_2)^{1/2} + \epsilon_1]^{1/2} \qquad (C.23)$$

$$k = \frac{1}{\sqrt{2}}[(\epsilon_1 + \epsilon_2)^{1/2} - \epsilon_1]^{1/2} \tag{C.24}$$

A set of equations for the dielectric function $\epsilon(\omega)$ and complex conductivity $\sigma(\omega)$ can be found, when we model the electrons within the dielectric material as a set of damped oscillators. Solving the equation of motion will yield following relation for the complex index of refraction

$$N^2 = 1 - \frac{\sigma_{dc}\gamma}{\epsilon_0} \frac{1}{\omega^2 - \omega_0^2 + i\gamma\omega} \tag{C.25}$$

where σ_{dc} is the dc conductivity (at $\omega = 0$). The complex conductivity is related to the complex index of refraction, according to:

$$N^2 = 1 - i\frac{\sigma(\omega)}{\epsilon_0\omega}. \tag{C.26}$$

In the case of a metal, eqn. C.25 will change slightly by setting ω_0 to zero, however the general result C.26 remains valid. Now taking into account equation C.20 we have

$$\epsilon_1 = n^2 - k^2 = 1 - \frac{\sigma_2}{\epsilon_0\omega} \tag{C.27}$$

$$\epsilon_2 = 2nk = \frac{\sigma_1}{\epsilon_0\omega} \tag{C.28}$$

(Here, we still think of $\mu_{rel} = 1$. At infrared frequencies the magnetic permeability μ_r may usually be assumed equal to unity [14].)

C.1   Reflection at Normal Incidence

The reflectance of light at normal incidence onto an ideal solid surface can be derived simply from a consideration of the boundary conditions for **E** and **H** at the interface [48]. For the electric field strengths we can write

$$E_i + E_r = E_t \tag{C.29}$$

where subscripts i, r and t represent, respectively, the incident, reflected and transmitted waves at the interface. A similar equation holds for H, but with a change in sign for H_r

$$H_i - H_r = H_t \tag{C.30}$$

(Here, we must remember that **H** is perpendicular to **E** in the sense, that **E** × **H** is in the direction of propagation.) In the vacuum, $H = (1/c\mu_0)E$ (or $H = \sqrt{\epsilon_0/\mu_0}E$), whereas in the medium

$$H = (\frac{\epsilon_0 cN}{\sqrt{\mu_{rel}}})E, \tag{C.31}$$

where c is the speed of light and we assume $N = \sqrt{\epsilon}$.

Thus, equations C.29 and C.30 become

$$E_i + E_r = E_t \tag{C.32}$$

$$E_i - E_r = NE_t \tag{C.33}$$

where the relative permeability μ_{rel} has been taken as unity. Equations C.32 and C.33 are easily solved to yield a reflectivity coeffiecient

$$r = \frac{E_r}{E_i} = \frac{1-N}{1+N} \tag{C.34}$$

The reflectance is then given by

$$R = r^*r = (\frac{1-N}{1+N})^2 = \frac{(1-n)^2 + k^2}{(1+n)^2 + k^2} \tag{C.35}$$

Generally, the reflectivity coefficient is a complex number, so we can write

$$r(\omega) = \rho(\omega)e^{i\theta(\omega)} \tag{C.36}$$

or

$$r(\omega) = \rho(\omega)(\cos\theta + i\sin\theta) \tag{C.37}$$

where we have separated the amplitude $\rho(\omega) = \sqrt{R(\omega)}$ and the phase $\theta(\omega)$ parts. Now knowing that

$$r(\omega) = \frac{1 - n - ik}{1 + n + ik} = \rho(\omega)(\cos\theta + i\sin\theta) \tag{C.38}$$

$$r^*(\omega) = \frac{1 - n + ik}{1 + n - ik} = \rho(\omega)(\cos\theta - i\sin\theta) \tag{C.39}$$

$$R = \frac{(1 - n)^2 + k^2}{(1 + n)^2 + k^2} = 1 - \frac{4n}{(n + 1)^2 + k^2} \tag{C.40}$$

by adding and subtracting equations C.38 and C.39 and using C.40 we are able to find out

$$k = \frac{2\sqrt{R}\sin\theta}{1 - 2\sqrt{R}\cos\theta + R} \tag{C.41}$$

$$n = \frac{1 - R}{1 - 2\sqrt{R}\cos\theta + R} \tag{C.42}$$

which relate the complex refractive index to the reflectance, after the phase has been determined by means of the Kramers-Kronig analysis (see Chapter 2).

Bibliography

[1] E. V. Loewenstein, *The History and Current Status of Fourier Transform Spectroscopy*, Applied Optics, **5**, p. 845, (1966).

[2] A. G. Marshall and F. R. Verdun, *Fourier Transforms in NMR, Optical and Mass Spectrometry*, Elsevier Science Publishers B.V., Amsterdam, (1990).

[3] www.wikipedia.org/wiki/Fourier_Transform_Spectroscopy

[4] R. Williams, *Spectroscopy and the Fourier Transform (An Interactive Tutorial)*, VCH Publishers, New York, (1996).

[5] Ch. P. Schultz, *Precision Infrared Spectroscopy Imaging*, Bruker Optics, www.brukeroptics.com/downloads/SP1001Schultz.pdf

[6] http://scienceworld.wolfram.com/physics/FourierTransformSpectrometer.html

[7] www.oriel.com/down/pdf/05004.pdf, Introduction to FT-IR Spectroscopy, Oriel Instruments

[8] P. R. Griffiths and J. A. de Haseth, *Fourier Transform Infrared Spectrometry*, John Wiley & Sons, New York, (1986).

[9] Ch. Kittel, *Introduction to Solid State Physics*, 7th edition, John Wiley and Sons, NY, (1996).

[10] D. Krcho, *Kramers-Kronig Relations in Fourier Transform Infrared Spectroscopy of Semiconductors*, http://www.pv.unsw.edu.au/miscpapers/kramerskronig.pdf

[11] L. D. Landau and E. M. Lifshitz, *Electrodynamics of continuous media*, Pergamon Press, Oxford, (1960).

[12] M. Hildebrand, MSc. Thesis. Brock University, (1999).

[13] www.stanford.edu/class/ee243/ee243_02_appa_kk.pdf; D. A. B. Miller, *Proof of the Kramers-Kronig relations*

[14] J. T. Houghton and S. D. Smith, *Infra-red Physics*, Oxford University, (1966).

[15] J. N. Hodgson, *Optical absorption and dispersion in solids*, Buttler & Tanner Ltd., (1970).

[16] A. D. Slepkov, B.Sc. Thesis, Brock University (1999).

[17] Infrared Laboratories, *Brock University Instruction Mannual*, (1995).

[18] http://www.encyclopedia.com/html/b1/bolomete.asp

[19] http://www.tpub.com/neets/book16/67a.htm

[20] L. J. van der Pauw, *A method of measuring specific resitivity and Hall effect of discs of arbitrary shape*, Philips Research Reports 13, (1958).

[21] J.C. Slater and N.H. Frank, *Electromagnetism*, McGraw-Hill Book Company Inc.,New York and London,(1947).

[22] A.B. Holden, MSc. Thesis, Brock University, (2001).

[23] P.A. Lee, T.M. Rice, J.W. Serene, L.J. Sham and J.W. Wilkins, *"Theories of Heavy-Electron Systems"*, Science **12**, No. 3, p. 99, (1986).

[24] http://physics.ucsd.edu/~pietri/Contents/Resume/research.html

[25] http://education.jlab.org/beamsactivity/6thgrade/tableofelements/index.html

[26] Z. Fisk, D.W. Hess, C.J. Pethick, D. Pines, J.L. Smith, J.D. Thompson, J.O. Willis, *"Heavy-Electron Metals: New Highly Correlated States of Matter"*, Science **239**, pp 33-42, (1988).

[27] K. Andres, J.E. Graeber and H.R. Ott, Phys. Rev. Lett **35**, p. 1779, (1975).

[28] C. Petrovic, P.G. Pagliuso, M.F. Hundley, R. Movshovich, J.L. Sarrao, J.D. Thompson, Z. Fisk and P. Monthoux, *"Heavy-fermion superconductivity in $CeCoIn_5$ at 2.3K"*, J. Phys.: Condens. Matter **13**, L337, (2001).

[29] F. Steglich, J. Aarts, C.D. Bredl, W. Lieke, D. Meschede, W. Franz and H. Schafer, Phys. Rev. Lett. **43**, p. 1892, (1979).

[30] C. Petrovic, R. Movshovich, M. Jaime, P.G. Pagliuso, M.F. Hundley, J.L. Sarrao, Z. Fisk and J.D. Thompson, *"A new heavy-fermion superconductor $CeIrIn_5$: A relative of the cuprates?"*, Europhys. Lett. **53**, p. 354, (2001).

[31] T.P. Murphy, D. Hall, E.C. Palm, S.W. Tozer, C. Petrovic, Z. Fisk, R.G. Goodrich, P.G. Pagliuso, J.L. Sarrao and J.D. Thompson, *"Anomalous Superconductivity and Field-Induced Magnetism in $CeCoIn_5$"*, Phys. Rev. B **65**, 100514, (2002).

[32] N.D. Mathur, F.M. Grosche, S.R. Julian, I.R. Walker, D.M. Freye, R.K.W. Haselwimmer and G.G. Lonzarich, *"Magnetically mediated superconductivity in heavy fermion compounds"*, Nature **394**, (1998).

[33] J. Costa-Quintana and F. Lopez-Aguilar, *"Electronic structure of $CeCoIn_5$"*, Phys. Rev. B **67**, 132507, (2003).

[34] R. Movshovich, M. Jaime, J.D. Thompson, C. Petrovic, Z. Fisk, P.G. Pagliuso and J.L. Sarrao, *"Unconventional Superconductivity in $CeIrIn_5$ and $CeCoIn_5$: Specific Heat and Thermal Conductivity Studies"*, Phys. Rev. Lett. **86**, p. 5152, (2001).

[35] I.R. Walker, F.M. Grosche, M.D. Freye and G.G. Lonzarich, Physica C **282**, p. 303, (1997).

[36] E.E.M. Chia, D.J. Van Harlingen, M.B. Salamon, B.D. Yanoff, I. Bonalde and J.L. Sarrao, *"Nonlocality and strong coupling in the heavy fermion superconductor CeCoIn$_5$: A penetration depth study"*, Phys. Rev. B **67**, 014527, (2003).

[37] S. Ozcan, D.M. Broun, B. Morgan, R.K.W. Haselwimmer, J.R. Waldram, J.L. Sarrao, S. Kamal, C.P. Bidinosti and P.J. Turner, *"CeCoIn$_5$ - a quantum critical superfluid?"*, arXiv:cond-mat/0206069 v1, (2002).

[38] E.J. Singley, D.N. Basov, E.D. Bauer and M.B. Maple, *"Optical conductivity of the heavy fermion superconductor CeCoIn$_5$"*, Phys. Rev. B **65**, 161101, (2002).

[39] J.S. Kim, J. Alwood, G.R. Stewart, J.L. Sarrao and J.D. Thompson, *"Specific heat in high magnetic fields and non-Fermi-liquid behaviour in CeMIn$_5$ (M = Ir, Co)*, Phys. Rev. B **64**, 134524, (2001).

[40] Y. Bang and A.V. Balatsky, *"Anomalous specific heat jump in the heavy fermion superconductor CeCoIn$_5$"*, arXiv:cond-mat/0303447 v1, (2003).

[41] R.J. Ormeno, A. Sibley, C.E. Gough, S. Sebastian and I.R. Fisher, *"Microwave conductivity and Penetration Depth in the Heavy Fermion Supercodnuctor CeCoIn$_5$"*, Phys. Rev. Lett. **88**, 047005, (2002).

[42] D. Hall, E. Palm, T. Murphy, S. Tozer, Z. Fisk, U. Alver, R.G. Goodrich, J.L. Sarrao, P.G. Pagliuso and T. Ebihra, *"The Fermi surface of CeCoIn$_5$: dHvA"*, arXiv:cond-mat/0102533 v1, (2001).

[43] E.G. Moshopoulou, J.L. Sarrao, P.G. Pagliuso, N.O. Moreno, J.D. Thompson, Z. Fisk and R.M. Ibberson, *"Comparison of the Crystal Sructure of the Heavy-Fermion Materials CeCoIn$_5$, CeRhIn$_5$ and CeIrIn$_5$"*, Appl. Physics A, ICNS2001, (2002).

[44] http://www.physics.ubc.ca/ supercon/ciar/tanatar.pdf

[45] D. Hall, E. Palm, T. Murphy, S. Tozer, E. Miller-Ricci, L. Peabody, Ch. Q. H. Li, U. Alver, R.G. Goodrich, J.L. Sarrao, P.G. Pagliuso, J.M. Wills and Z. Fisk, *"Electronic Structure of CeRhIn$_5$: dHvA and Energy Band Calculations"*, arXiv:cond-mat/0011395 v1, (2000).

[46] http://mathworld.wolfram.com/FourierSeries.html

[47] J. H. Mathews and R. W. Howell, *Complex Analysis for Mathematics and Engineering*, WCB, (1996).

[48] F. Wooten, *Optical Properties of Solids*, Academic Press, New York, (1972).

[49] M. Dressel and G. Gruner, *Electrodynamics of Solids*, Cambridge University Press, (2002).

[50] P.M.C. Rourke, J. Berdeklis, C.S. Turel, M. Tanatar and C. Petrovic, *Point-Contact Specroscopy Study of CeCoIn$_5$*, Presentation for APS March Conference, Montreal, (2004), **unpublished.**

[51] M. Reedyk, Ph.D., private communication.

[52] D.A. Bonn, J.D. Garrett and T. Timusk, *Far-Inrared Properties of URu$_2$Si$_2$*, Phys. Rev. Lett. **61**, No. 11, (1998).

[53] V.A. Sidorov, M. Nicklas, P.G. Pagliuso, J.L. Sarrao, Y. Bang, A.V. Balatsky and J.D. Thompson, *Superconductivity and Quantum Criticality in CeCoIn$_5$*, Phys. Rev. Lett. **89**, No. 15, (2002).

[54] A. Bianchi, R. Movshovich, I. Vekhter, P.G. Pagliuso and J.L. Sarrao, *Avoided Antiferromagnetic Order and Quantum Critical Point in CeCoIn$_5$*, Phys. Rev. Lett. **91**, No. 25, (2003).

[55] S. Chakravarty, Ch. Nayak, S. Tewari and X. Yang, *Sharp Signature of a $d_{x^2-y^2}$ Quantum Critical Point in the Hall Coefficient of Cuprate Superconductors*, Phys. Rev. Lett. **89**, No. 27, (2002).